Simulations of oscillatory binary fluid convection in large aspect ratio containers

Oriol Batiste,[1] Edgar Knobloch,[2] Isabel Mercader,[1] and Marta Net[1]
[1]*Departament de Física Aplicada, Universitat Politècnica de Catalunya, 08034 Barcelona, Spain*
[2]*Department of Physics, University of California, Berkeley, California 94720*
(Received 8 June 2001; published 14 December 2001)

Direct numerical simulations of chevrons, blinking states, and repeated transients in binary fluid mixtures with a negative separation ratio heated from below are described. The calculations are performed in two-dimensional containers using realistic boundary conditions and the parameter values used in the experiments of Kolodner [Phys. Rev. E **47**, 1038 (1993)]. Particular attention is paid to the multiplicity of states, and their dependence on the applied Rayleigh number and the aspect ratio of the container. Quantitative agreement with the experiments is obtained, and a mechanism explaining the origin and properties of the repeated transients observed in the experiments is proposed.

DOI: 10.1103/PhysRevE.65.016303 PACS number(s): 47.20.Bp, 47.20.Ky, 47.27.Te, 41.20.Jb

I. INTRODUCTION

Binary fluid mixtures exhibit a wide variety of behavior when heated from below. Of particular interest are mixtures with a negative separation ratio. If the separation ratio is sufficiently negative, the conduction state undergoes a Hopf bifurcation with increasing Rayleigh number, creating a wide variety of traveling wave states at finite amplitude. In the present paper, we are particularly interested in understanding the states observed in rectangular containers of moderately large aspect ratio, including the so-called ''chevron'' and ''blinking'' states [1,2]. The ''chevrons'' (or counterpropagating waves) consist of a pair of equal amplitude waves propagating (usually) outwards from the cell center; when the amplitudes of these waves oscillate about the equal amplitude state the pattern is dominated alternately by left- and right-traveling waves and is then called a ''blinking'' state. The blinking states were first observed in simulations of doubly diffusive convection [3], and subsequently in experiments on binary fluid convection [4,5]. In contrast to the chevrons, which have been observed in experiments only rarely [2], the blinking states appear to be much more robust. Both these states owe their existence to the presence of sidewalls, and may be understood on the basis of both bifurcation theory [6] and Ginzburg-Landau theory [7]. Of particular interest in the present paper is a third state, the ''repeated transients,'' observed by Kolodner and and co-workers [1,5,8] in water-ethanol mixtures. These states consist of chevrons that grow exponentially from small amplitude without change of shape until they reach a critical amplitude at which they become unstable and collapse back to small amplitude. The experiments reveal that the dynamics of these states depend sensitively on the aspect ratio of the system, and on the Rayleigh number. Understanding of the repeated transients appears to lie outside of the Ginzburg-Landau type of description employed in [7].

The existing experiments [1,2,8] raise a number of interesting and important theoretical questions. These include:

(i) What is the nature of the saturated state into which the initial instability develops?

(ii) What is the origin of the sensitive dependence of the final state on the aspect ratio Γ of the container, and on the Rayleigh number R?

(iii) What is the mechanism by which stable chevrons turn into blinking states and/or repeated transients?

(iv) How do the repeated transients and the blinking states disappear?

(v) Is there hysteresis at the onset of the repeated transients?

Despite much experimental effort that has gone into answering these types of questions the situation remains far from clear. To date, the most thorough study of a number of these issues is the paper by Kolodner [8]. This paper presents a great deal of valuable information about the dynamical behavior near onset, but even with this information the basic picture remains clouded. In particular, the basic mechanism responsible for the experimental results remains elusive. In this paper, we set out to answer as many of the above questions as possible. Our approach involves experiments of a different kind, namely, direct numerical simulations of the partial differential equations. Consequently, we focus on the parameter values used by Kolodner [8], and integrate the governing equations in two dimensions, using realistic boundary conditions on the four sides of the container. Using the results of these simulations, we are able to answer a number of the outstanding questions. In particular, we are able to uncover a deterministic mechanism that provides a unified and coherent picture of the transitions between chevrons, blinking states, and repeated transients, and that is consistent with the results of all our simulations. This mechanism is fundamentally low-dimensional, indicating that even extended systems may behave as low-dimensional systems sufficiently close to onset. In certain cases, our numerical results disagree in detail with Kolodner's experiments. In these cases, we are able to make clear and precise predictions that would confirm the basic dynamical systems mechanism we put forward. Some of our results have already been reported [9].

The paper is organized as follows. In Sec. II we introduce the equations we solve. Section III summarizes the results of the simulations, followed in Sec. IV by a description of the mechanism that accounts for them. The paper concludes with

a brief summary of our results and their implications for the experiments. Some of the more mathematical aspects of our discussion have been relegated to a couple of appendixes.

II. BASIC EQUATIONS

Binary fluid mixtures are characterized by the presence of cross-diffusion terms in the diffusion matrix. In water-ethanol mixtures, the dominant cross-diffusion term is the Soret term. The sign of the Soret coefficient determines the behavior of the mixture in response to an applied temperature gradient. In mixtures with a negative Soret coefficient the heavier component migrates towards the hotter boundary, i.e., a concentration gradient is set up that opposes the destabilizing temperature gradient that produced it. Under these conditions, the onset of convection may take the form of growing oscillations. This is the situation that is of interest here.

We consider a binary mixture in a two-dimensional rectangular container $D \equiv \{x,z | 0 \leqslant x \leqslant \Gamma, -\frac{1}{2} \leqslant z \leqslant \frac{1}{2}\}$ heated uniformly from below. We nondimensionalize the equations using the depth of the layer as the unit of length and t_d, the vertical thermal diffusion time, as the unit of time. In the Boussinesq approximation appropriate to the experiments, the resulting equations take the form [10]

$$\partial_t \mathbf{u} + (\mathbf{u}\cdot\boldsymbol{\nabla})\mathbf{u} = -\boldsymbol{\nabla} P + \sigma R[\theta(1+S) - S\eta]\hat{\mathbf{z}} + \sigma\nabla^2\mathbf{u}, \tag{2.1a}$$

$$\partial_t \theta + (\mathbf{u}\cdot\boldsymbol{\nabla})\theta = w + \nabla^2\theta, \tag{2.1b}$$

$$\partial_t \eta + (\mathbf{u}\cdot\boldsymbol{\nabla})\eta = \tau\nabla^2\eta + \nabla^2\theta, \tag{2.1c}$$

together with the incompressibility condition

$$\boldsymbol{\nabla}\cdot\mathbf{u} = 0. \tag{2.1d}$$

Here $\mathbf{u} \equiv (u,w)$ is the velocity field in (x,z) coordinates, P is the pressure, and θ denotes the departure of the temperature from its conduction profile in units of the imposed temperature difference ΔT. The variable η is defined such that its gradient represents the dimensionless mass flux. Thus, $\eta \equiv \theta - C$, where C denotes the concentration of the heavier component relative to its conduction profile, scaled with the concentration difference that develops across the layer as a result of the Soret effect. The system is specified by four dimensionless parameters: the separation ratio S that measures the strength of the Soret effect, the Rayleigh number R providing a dimensionless measure of the imposed temperature difference ΔT, and the Prandtl and Lewis numbers σ, τ, in addition to the aspect ratio Γ.

The boundary conditions adopted will be those relevant to the experiments. Thus, we take the boundaries to be no-slip everywhere, with the temperature fixed at the top and bottom and no sideways heat flux. The final set of boundary conditions is provided by the requirement that there be no mass flux through any of the boundaries. The boundary conditions are thus

$$\mathbf{u} = \mathbf{n}\cdot\boldsymbol{\nabla}\eta = 0 \quad \text{on } \partial D, \tag{2.2}$$

and

$$\theta = 0 \quad \text{at } z = \pm 1/2, \quad \partial_x\theta = 0 \quad \text{at } x = 0, \Gamma. \tag{2.3}$$

Here ∂D denotes the boundary of D.

Although the above problem has been tackled by several authors [11], the results obtained thus far are incomplete, and the calculations were often not carried on for long enough to equilibrate properly. We show below that the above system possesses in general very long transients, requiring considerable patience in order to obtain reliable results. Rather more progress has been made on the related (but simpler) problem in which the lateral boundary conditions are replaced by periodic boundary conditions [12] or by artificial reflective boundary conditions to mimic the presence of lateral boundaries [12,13]. These studies have clarified the role of the concentration distribution in traveling wave states, and identified spatially localized traveling wave states, i.e., states consisting of waves propagating under a stationary envelope attached to one of the boundaries. Our calculations confirm these results. However, the aim of the present paper is more ambitious, in that we focus on states with nontrivial dynamics, and do so with realistic lateral boundary conditions.

We solve Eqs. (2.1)–(2.3) using a time-splitting method with an improved boundary condition for the pressure as described in Ref. [14]. The time integration scheme is second-order accurate and is based on a modified Adams-Bashforth formula [14]. For the spatial discretization, we use a Chebyshev collocation pseudospectral method [15]. In all cases, the time step and the number of collocation points used was adjusted until the solutions converged. Typically, we used 170 collocation points in the x direction and 30 collocation points in the z direction, with a time step of 10^{-3} (in units of the vertical diffusion time).

Equations (2.1)–(2.3) are equivariant with respect to the operations

$$R_x : (x,z) \to (\Gamma - x, z), \quad (\psi, \theta, C) \to (-\psi, \theta, C), \tag{2.4}$$

$$\kappa : (x,z) \to (x, -z), \quad (\psi, \theta, C) \to (-\psi, -\theta, -C), \tag{2.5}$$

where $\psi(x,z,t)$ is the stream function, defined by $(u,w) = (-\psi_z, \psi_x)$. These two operations generate the symmetry group D_2 of a rectangle. Bifurcation theory shows that in this case, the eigenfunctions of the linear stability problem for the conduction state $\mathbf{u} = \theta = \eta = 0$ must be either even or odd under reflection in $x = \Gamma/2$. As a consequence, only branches of even and odd solutions may bifurcate from the conduction state [6]. Specifically, the even eigenfunctions are invariant under R_x, i.e.,

$$(\psi(x,z), \theta(x,z), C(x,z)) = (-\psi(\Gamma - x, z), \theta(\Gamma - x, z), C(\Gamma - x, z))$$

at each instant in time, while the odd eigenfunctions are invariant under κR_x, i.e.,

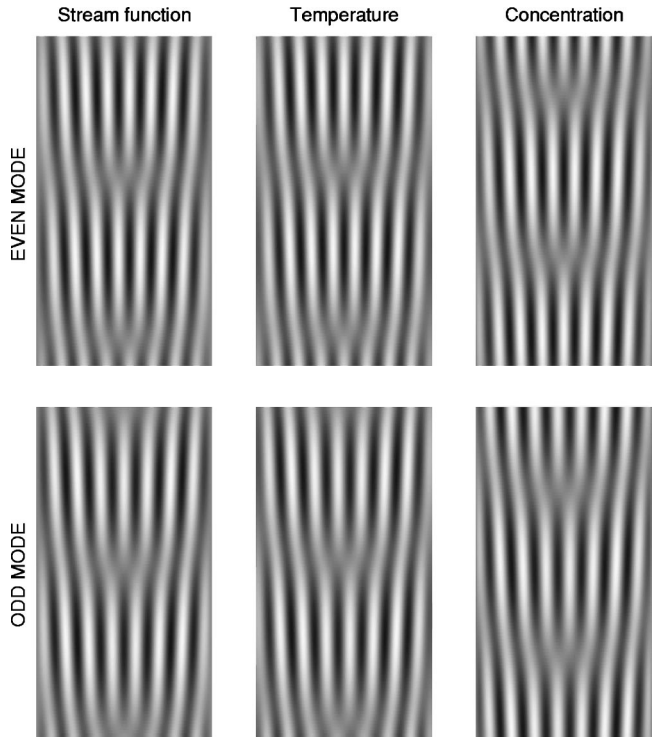

FIG. 1. The eigenfunction (ψ,θ,C) of the linear stability problem for $\Gamma=16.25$, $S=-0.021$, $\sigma=6.97$, $\tau=0.0077$, and (a) $R_c=1776.30$, $\omega_c=2.819$ (even chevron), (b) $R_c=1787.47$, $\omega_c=2.686$ (odd chevron), shown in the form of space-time diagrams at $z=0$ with $0\leqslant x\leqslant\Gamma$ drawn horizontally and time increasing upwards. The solutions are sinusoidal with period $2\pi/\omega_c$.

$$(\psi(x,z),\theta(x,z),C(x,z)) = (\psi(\Gamma-x,-z),-\theta(\Gamma-x,-z), -C(\Gamma-x,-z)),$$

again at each instant of time. Note that at midlevel, $z=0$, the odd eigenfunction is odd in the conventional sense, i.e., R_x changes the sign of each component of the vector (ψ,θ,C). Consequently, the eigenfunction in the midplane is also invariant under R_x followed by evolution through half the Hopf period. Explicit solution of the linear stability problem [16] indicates that the competition between even and odd modes in such a system takes one of two basic forms, depending on the separation and aspect ratios. When $|S|$ is small (i.e., close to $|S_{TB}|$, the Takens-Bogdanov point) and Γ not too large, the mode interaction takes the form familiar from Rayleigh-Bénard convection with non-Neumann boundary conditions: the neutral curves $R_c(\Gamma)$ divide neatly between different families with no intermingling among them. Each family consists of a pair of braided neutral curves, one for an odd mode and the other for an even mode, with each family well separated from the next, at least for the low-lying families. The crossings between odd and even modes within each family are structurally stable because of their different parity. For the case of interest in the present paper, i.e., Γ and $|S|$ large enough, the situation is quite different. There are now no distinct families of neutral curves and all modes (including like-parity modes) cross. These mode crossings are all structurally stable, either because the modes have opposite parity, or because their frequencies at the mode crossing are nonresonant. The transition between these two situations is discussed in detail in [16].

In Figs. 1 and 2, we show the results of solving this linear problem for $S=-0.021$, $\sigma=6.97$, and $\tau=0.0077$, corresponding to the experimental mixture used by Kolodner [8]. Depending on the aspect ratio, the critical eigenfunction takes the form of either an even or an odd parity ''chevron,'' shown in Fig. 1 in the form of space-time diagrams for the three fields (ψ,θ,C) evaluated at $z=0$. An even parity chevron consists of waves propagating outwards from a source at the center of the cell in such a way that the resulting solution is symmetric at all times with respect to reflection about $x=\Gamma/2$. In contrast, as discussed above, an odd parity chevron (at $z=0$) is at all times odd with respect to this reflection. Note that, despite appearances, these solutions are *strictly sinusoidal* in time: the periodic defect formation at $x=\Gamma/2$ arises because the eigenfunction ψ is a superposition of four functions each of which has the form $\psi_j\exp[i(\omega_c t\pm k_j x)]$, $j=1,\ldots,4$, with the k_j possibly complex. Each of these functions describes waves propagating with (local) phase velocity $\pm\omega_c/\mathrm{Re}\,k_j$. In the bulk, the eigenfunction is dominated by the largest contribution; this contribution has a real wave number and describes oscillations that are almost standing. However, when the time-dependent amplitude of this component passes through zero (which occurs twice per period) the remaining contributions briefly reveal themselves. In the eigenfunctions shown, the largest of these has a relatively large phase velocity, and is responsible for the episodic propagation that is so characteristic of these eigenfunctions. The other two fields oscillate in the same manner, but with a temporal phase lag relative to ψ that is determined by the values of the Prandtl and Lewis numbers used. Note also that, despite the nonuniformity in the amplitude of the eigen-

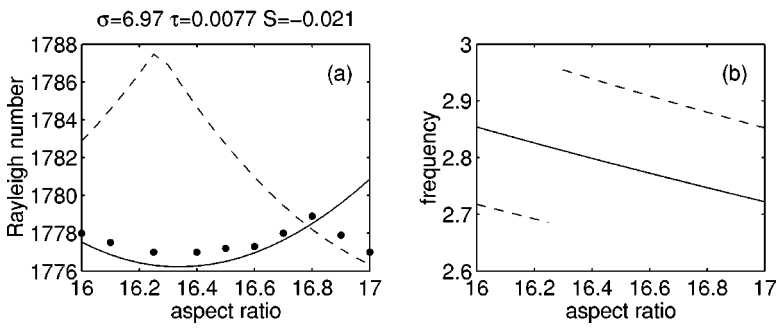

FIG. 2. (a) The critical Rayleigh number R_c and (b) the corresponding frequency ω_c for $S=-0.021$, $\sigma=6.97$, and $\tau=0.0077$ as a function of the aspect ratio Γ. Solid (broken) lines indicate even (odd) parity chevrons. The solid dots correspond to the solutions shown in Fig. 3.

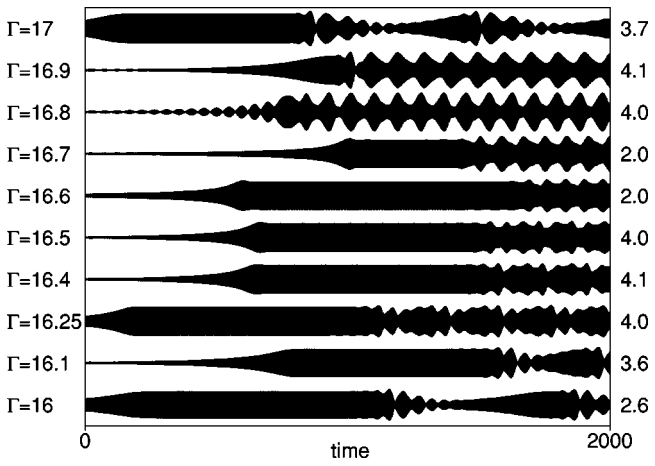

FIG. 3. An overview of the aspect ratio dependence of the equilibrated states near onset, in terms of the vertical velocity $w(x=0.13\Gamma,z=0,t)$ for comparison with Fig. 2 of Ref. [8]. The numbers at the right give the values of $10^4\epsilon$ and correspond to the solid dots in Fig. 2(a).

function in x, the dominant local wave number is in fact remarkably uniform across the cell.

The critical Rayleigh numbers R_c for the onset of these states are shown in Fig. 2(a), with the even modes indicated by solid lines, and the odd modes by broken lines. The corresponding critical frequencies ω_c are shown in Fig. 2(b). Figure 2(a) shows two neutral stability curves corresponding to two different odd modes, with an intersection near $\Gamma=16.25$, as well as an intersection between an odd and even mode near $\Gamma=16.8$. The latter mode interaction is accessible from the conduction state and will play an important role in the dynamics of the system. Note that both mode interactions are associated with a frequency jump if one always follows the low-lying mode.

Throughout the remainder of the paper, we measure the applied Rayleigh number relative to the threshold R_c using the reduced Rayleigh number $\epsilon\equiv(R-R_c)/R_c$.

III. RESULTS

In this section, we describe in detail the results of our simulations for the parameter values used by Kolodner [8] in his experiments, $S=-0.021$, $\sigma=6.97$, and $\tau=0.0077$, focusing on Rayleigh numbers near threshold (i.e., $|\epsilon|\ll 1$) and on aspect ratios in the range $16\leqslant\Gamma\leqslant 17$.

Figure 3 summarizes the evolution for different values of Γ of the midplane vertical velocity $w(x=0.13\Gamma,z=0,t)$ obtained by integration over $2000t_d$ after an initial transient has (almost) died out. We use the velocity at this point as a proxy for the intensity measured by Kolodner in his experiments, since the temporal properties of the corresponding time series will be the same, although amplitudes and spatial structure will not be so simply related. The figure illustrates the sensitive dependence on the aspect ratio for comparison with Fig. 2 of [8], as well as the long integration times required to get reliable results. The high frequency uniform amplitude states correspond to nonlinear time-periodic chevron states such as the one shown in Fig. 4. In the following, we refer to

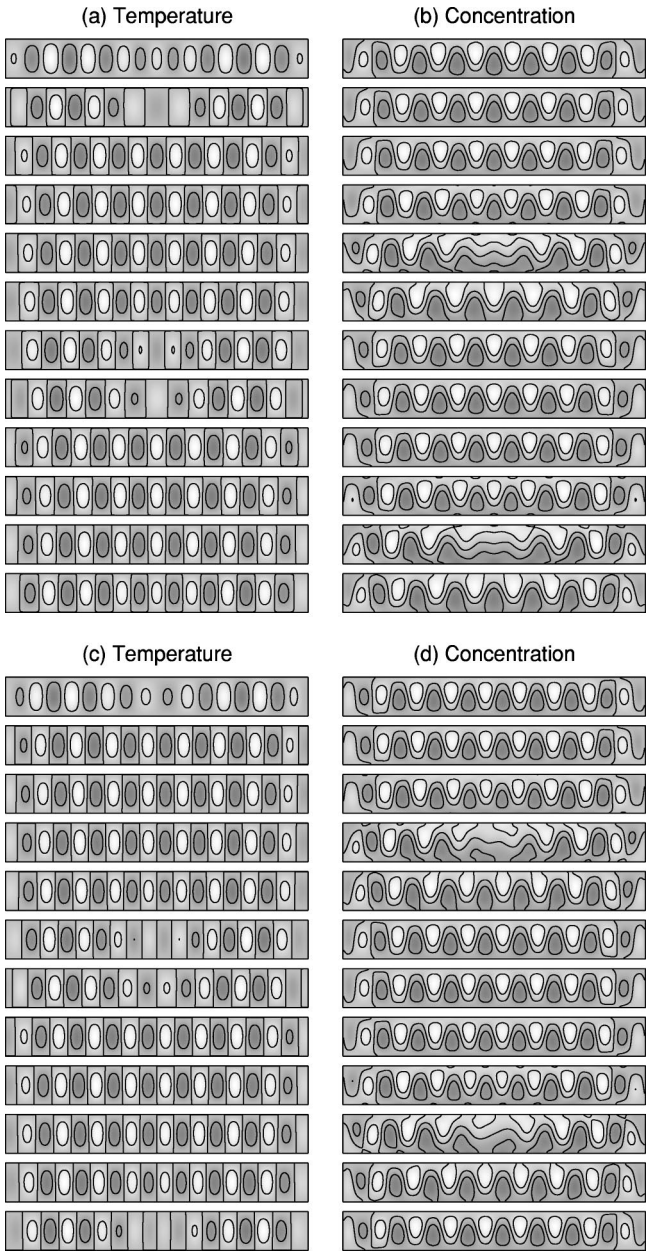

FIG. 4. Periodic even parity chevron for $\Gamma=16.25$, $R=1775.5$ ($\epsilon=-4.5\times10^{-4}$) in terms of the contours of (a) the temperature perturbation $\theta(x,z,t)$ and (b) the concentration perturbation $C(x,z,t)$ of the denser component, with time increasing upwards in intervals of $0.2t_d$. (c), (d) The same but for an odd parity chevron for $\Gamma=17.25$, $R=1774.3$ ($\epsilon=-5.2\times10^{-4}$). These nonlinear states should be compared with the linear theory eigenfunctions in Fig. 1.

the frequency of these states as ω_1. The figure shows that although the temperature departure θ from the conduction profile remains sinusoidal in space at this value of ϵ, this is not so for the concentration departure C. As explained by Barten *et al.* [12], this is a consequence of the small value of τ and the associated expulsion of concentration fluctuations from regions of closed streamlines in the (locally) commoving reference frame. This effect is also responsible for the presence of open contours separating regions of high and low concentration, in evident contrast to the closed contours of

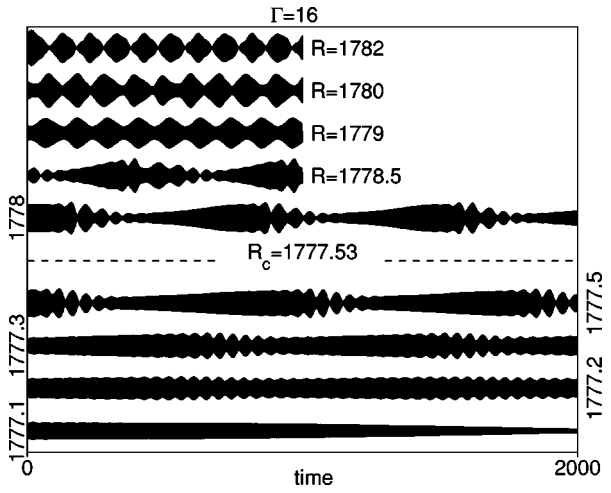

FIG. 5. Time series $w(x=0.13\Gamma, z=0,t)$ for $\Gamma=16.00$ and different values of the Rayleigh number R. The first finite amplitude state is a three-frequency state at $R=1777.2$ ($\epsilon=-1.8\times10^{-4}$). This state gives way gradually and without detectable hysteresis to repeated transient states near $\epsilon=0$ and then to symmetric periodic blinking states in a hysteretic transition between $R=1778.5$ ($\epsilon=5.5\times10^{-4}$) and $R=1779$ ($\epsilon=8.3\times10^{-4}$). The state at $R=1782$ ($\epsilon=2.5\times10^{-3}$) appears to have period-two modulation.

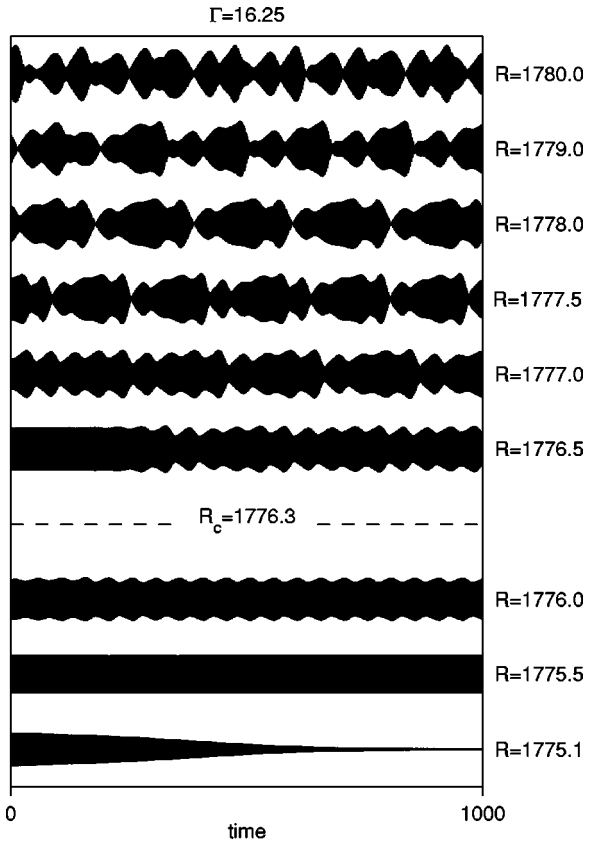

FIG. 6. Time series $w(x=0.13\Gamma, z=0,t)$ for $\Gamma=16.25$ and different values of the Rayleigh number R. Stable chevrons are present for $R=1775.5$ ($\epsilon=-4.5\times10^{-4}$), but give way to symmetric periodic blinking states when $R=1776$ ($\epsilon=-1.7\times10^{-4}$) with no detectable hysteresis. At larger R (e.g., $R=1778$) the blinking states are asymmetric.

the temperature (see Fig. 4). The temporary straightening of these meandering concentration contours in the cell center every half period accompanies the splitting of the central concentration roll into two. Both these properties of the concentration field are absent from the Ginzburg-Landau description of this system.

In order to understand the origin and character of the nonperiodic states seen in Fig. 3, we show in Figs. 5–9 the results of fixing Γ at 16.00, 16.25, 16.50, 16.80, and 17.00, and varying ϵ in the vicinity of $\epsilon=0$. We order these figures with increasing aspect ratio in order to highlight the effects that even small changes in Γ may have. These plots show that the initial bifurcation to the chevron state is in all cases subcritical (the dashed line across each figure indicates the corresponding linear stability threshold), in agreement with the prediction for *standing waves* in a horizontally unbounded layer [10,17]. Figure 6 for $\Gamma=16.25$ shows that the chevron state may equilibrate at finite amplitude ($R=1775.5$). However, with increasing ϵ, the stable chevrons lose stability in a supercritical Hopf bifurcation [18]. This bifurcation introduces a new frequency ω_{2k} into the system, seen in Fig. 6 ($R=1776.0$) as an oscillation in the amplitude of $w(x=0.13\Gamma, z=0,t)$. Consequently, the resulting state is in general quasiperiodic. In the following, we refer to the type of state that results as a ''blinking'' state. Such states may have a variety of spatiotemporal symmetries, and may set in already for $\epsilon<0$. Since the bifurcation in Fig. 6 is supercritical, the resulting blinking states blink with small amplitude and do so periodically; as ϵ increases the amplitude increases and the blinking becomes nonperiodic. In Fig. 10, we show a larger amplitude blinking state for $\Gamma=16.00$ and $R=1779$ (see Fig. 5). The figure shows the contours of the perturbation temperature $\theta(x,z)$ at two different instants, roughly half a blinking period apart, in order to show that the waves at these times are localized in opposite halves of the container. The figure also presents the time series for $w(x=0.13\Gamma, z=0,t)$ and $w(x=0.87\Gamma, z=0,t)$. Both time series have the same amplitude and form, and are, modulo the chevron frequency ω_1, exactly out of phase. In the following, we refer to solutions of this type as periodic symmetric blinking states. This type of description is possible here only because the frequency ω_1 is so large relative to the blinking frequency ω_2. This in turn is a consequence of the large aspect ratio that reduces the amplitude of the chevrons at which the bifurcation to the blinking states takes place [6]. We may therefore imagine averaging out the fast oscillations, and discuss the symmetry properties (and the time dependence) of the blinking component alone, without paying attention to the underlying chevron oscillation. In general, there are then two types of blinking states, depending on the parity of the chevron state from which they bifurcate. The blinking state in Fig. 6 arises from an even parity chevron, and so is left unchanged by the symmetry R_x followed by evolution in time through half the blinking period $2\pi/\omega_2$. In contrast, blinking states that bifurcate from an odd parity chevron are left invariant by the combined operation κR_x followed again by evolution in time through π/ω_2. We have found that monitoring the two point quantities

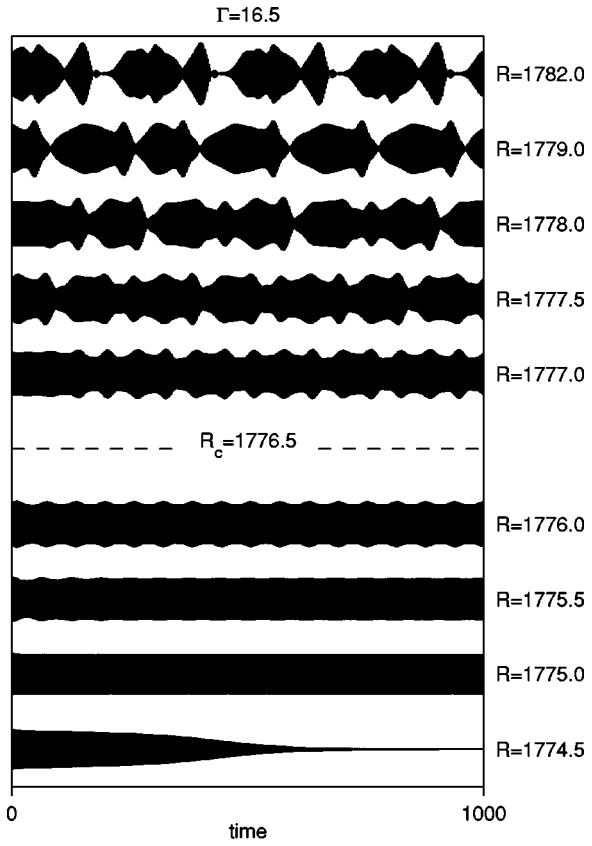

FIG. 7. Time series $w(x=0.13\Gamma, z=0,t)$ for $\Gamma=16.50$ and different values of the Rayleigh number R.

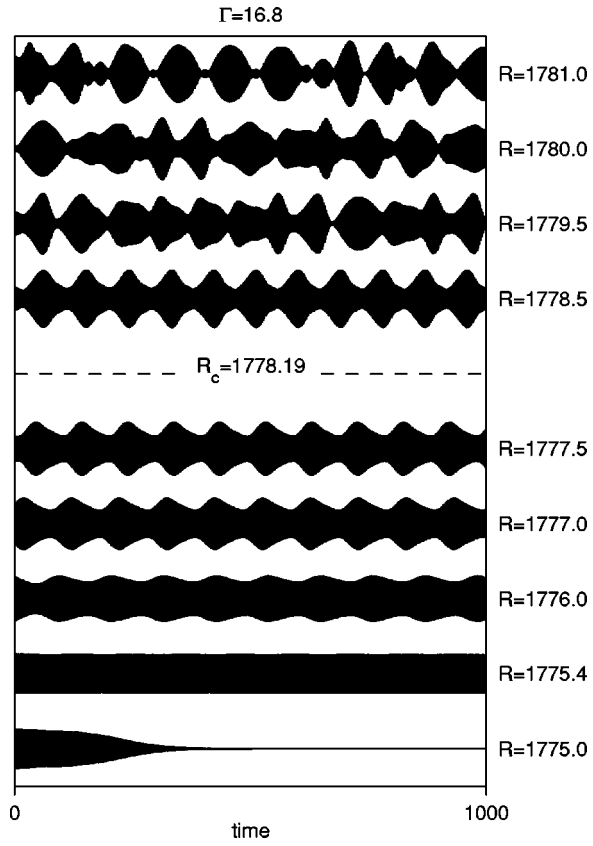

FIG. 8. Time series $w(x=0.13\Gamma, z=0,t)$ for $\Gamma=16.80$ and different values of the Rayleigh number R.

$w(x=0.13\Gamma, z=0,t)$ and $w(x=0.87\Gamma, z=0,t)$ sufficed in all cases to distinguish among the different types of blinking states.

The results for $\Gamma=16.00$ (Fig. 5) are quite different. In this case, no subcritical stable chevrons are observed, and instead the first nontrivial state of the system appears to be a three-frequency state ($R=1777.2$). We shall see in Sec. IV that such states are entirely natural in systems of this type. Figure 5 also shows that with increasing ϵ, this state evolves into one increasingly like Kolodner's repeated transients, with a growth phase that becomes progressively shorter, before a (hysteretic) transition to the symmetric periodic blinking state shown in Fig. 10 takes place ($1778.5<R<1779$). With further increase in ϵ, this state gradually evolves into a chaotically blinking state much as in Fig. 6. Indeed, the time series for $R=1782$ (Fig. 5) suggests a periodic state with a period that is double the basic blinking period. Figure 11 shows an example for $\Gamma=16.25$ in which the oscillations at the left and right are both periodic in time and of very similar form but with a phase difference between them that differs substantially from 180°. Since this phase difference remains constant, the resulting time series is quasiperiodic with two basic frequencies, the chevron frequency and the blinking frequency. As seen in Fig. 6, this type of state, hereafter an asymmetric periodic blinking state, develops with increasing ϵ from a symmetric blinking state, becoming chaotic as ϵ increases, much as observed in related experiments [1,2] and expected theoretically [19,20]. Other possibilities are dis-

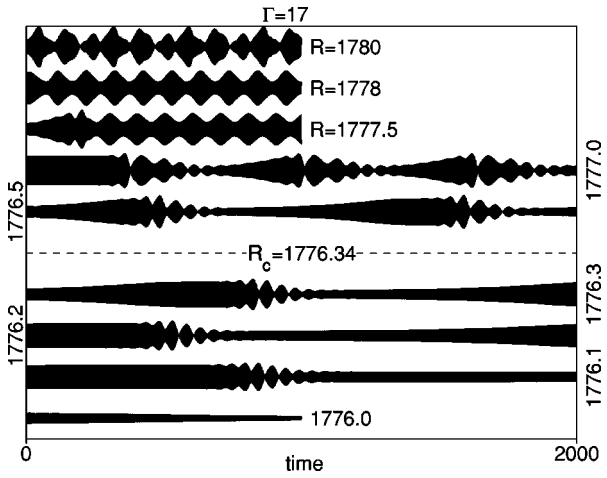

FIG. 9. Time series $w(x=0.13\Gamma, z=0,t)$ for $\Gamma=17.00$ and different values of the Rayleigh number R. The repeated transient state gives way to a periodic blinking state in a hysteretic transition between $R=1777$ ($\epsilon=3.7\times10^{-4}$) and $R=1777.5$ ($\epsilon=6.5\times10^{-4}$). The state at $R=1776.1$ ($\epsilon=-1.4\times10^{-4}$) eventually decays, while that at $R=1780$ ($\epsilon=2.1\times10^{-3}$) appears to have period-three modulation. The results follow closely the sequence shown in Fig. 5.

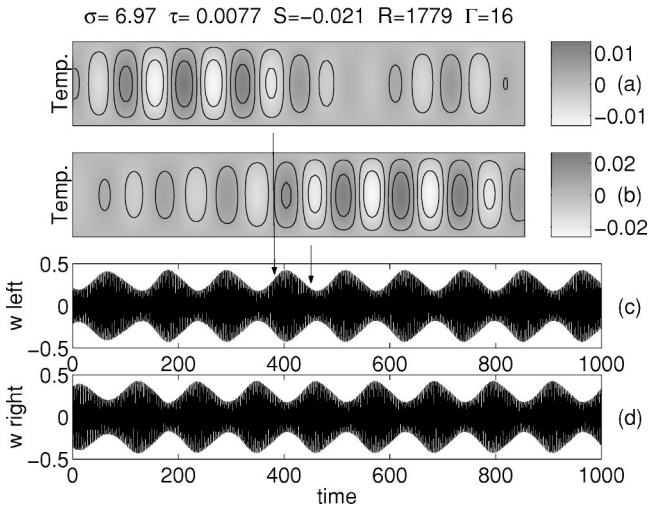

FIG. 10. Symmetric periodic blinking state for $\Gamma=16.0$ and $R=1779$ ($\epsilon=8.3\times10^{-4}$). For these parameter values $R_c=1777.528$, $\omega_c=2.854$. (a),(b) show the temperature field at two instants (indicated by vertical arrows), while (c),(d) show $w(x=0.13\Gamma, z=0,t)$ and $w(x=0.87\Gamma, z=0,t)$. The fact that (c), (d) are identical except for a 180° phase shift is indicative of a symmetric blinking state. The blinking period is approximately 0.4 of the horizontal thermal diffusion time.

cussed in Sec. IV. Note that despite the lack of instantaneous symmetry, the attractor shown in Fig. 11 is (almost) symmetric as a set, as are those that result from it, i.e., for these solutions, the behavior in the two halves of the container is almost (statistically) identical. However, this is not so for all the states we find, as described further below.

Stable subcritical chevrons were found for all the values of Γ explored except $\Gamma=16$ and 17. Figure 7, for $\Gamma=16.5$, shows results qualitatively similar to those shown in Fig. 6 with stable subcritical chevrons losing stability with increasing ϵ to symmetric periodic blinking states that become chaotic with further increase in ϵ. Figure 8 shows an example for $\Gamma=16.8$, a value very close to that for the interaction between the first even and the first odd parity modes in linear theory. The basic trend of the results remains the same as in Figs. 6 and 7 in that the stable chevron appears to lose stability at a supercritical Hopf bifurcation located at $\epsilon<0$, producing a symmetric periodic blinking state. The main effect of the proximity to the linear theory mode interaction point

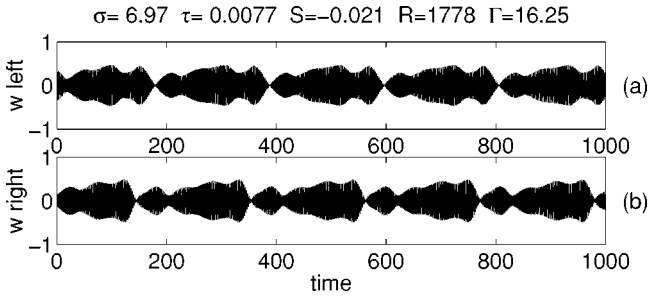

FIG. 11. An asymmetric periodic blinking state for $\Gamma=16.25$, $R=1778$ ($\epsilon=9.6\times10^{-4}$), showing (a) $w(x=0.13\Gamma, z=0,t)$ and (b) $w(x=0.87\Gamma, z=0,t)$.

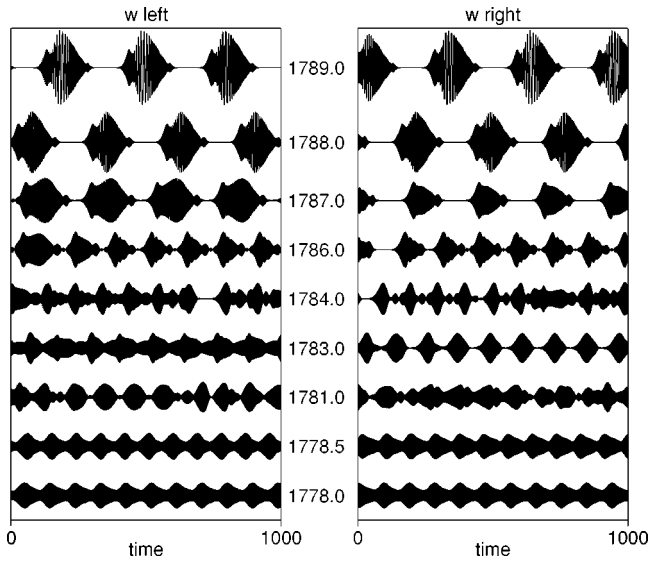

FIG. 12. Time series $w(x=0.13\Gamma, z=0,t)$ and $w(x=0.087\Gamma, z=o,t)$ for $\Gamma=16.80$ and larger values of the Rayleigh number R than in Fig. 8, showing successive transitions from asymmetric blinking states to symmetric ones and back again. The solutions at $R=1781$ and 1784 appear to be chaotic. Pauses, such as the one in the time series for $R=1784$, were observed in the experiments as well. [See Fig. 3(b) of Ref. [8].

at $\Gamma\approx16.8$ appears to be to extend the range of Rayleigh numbers over which stable blinking states are observed. In particular, stable symmetric periodic blinking states are now observed even for $\epsilon>0$. This is in accord with theoretical expectation (the onset of blinking is a consequence of the interaction between odd and even chevrons in the nonlinear regime), and accounts for the distinction between $\Gamma=16.8$ in Fig. 3 and other values of the aspect ratio. The blinking period we find, $\approx90t_d$, is comparable to the period measured in the experiments when $\Gamma=17.63$, viz. 8000 s, since $t_d=84.3$s [8] and the $\Gamma=17.63$ case behaves much like $\Gamma=16.63$ (for reasons explained below). In contrast, further away from the mode interaction point the range of stable periodic blinking states shrinks, and these states are typically found only for $\epsilon<0$. As a result, away from the mode interaction point the first state that is observed as ϵ passes through zero is a nonperiodic state, and not a periodic symmetric blinking state (cf. Figs. 6, 7). Of course, aspect ratios near $\Gamma=16.00$ or 17.00 are an exception to this rule. Figure 12 explores the evolution of the blinking states at larger values of ϵ when $\Gamma=16.8$ using time series for the vertical velocity at mirror points in the two halves of the container. The solutions are in general asymmetric with respect to the middle of the container, and may be periodic (as for $R=1783$, for example) or chaotic (as for $R=1784$). The figure also shows that with increasing ϵ, the left (right) traveling waves becomes increasingly confined to the left (right) half of the container, leading to characteristic time series of the type shown for $R=1787$ and 1788. Note that the former is strongly spatially asymmetric, while the latter is symmetric, with both states being periodic. Thus, transitions that break and restore the symmetry in the vertical midplane may occur

repeatedly, with the symmetric states at $R=1786$ and 1788 separated by an asymmetric one, suggesting the presence of a cascade of gluing bifurcations, cf. [21]. Note that the time series for $R=1789$ ($\epsilon=0.006$) is very similar to the "fish" state observed by Kolodner for $\Gamma=16.75$ and $\epsilon=0.0111$, even to the extent of capturing the strong amplitude dependence of the chevron frequency within this state. Moreover, the computed period of this state, $305t_d$ (see Fig. 12) corresponds almost exactly to that measured by Kolodner in the experiment.

Figure 9 shows the corresponding results for $\Gamma=17.00$. These results are very similar to those of Fig. 5 for $\Gamma=16.00$. In particular, one finds here the repeated transients, with a slow exponential growth of a pure parity chevron state, followed by its characteristic oscillatory collapse. In fact, the results for $\Gamma=17.00$ provide a somewhat clearer illustration of the origin of the three-frequency state, since they suggest that the oscillatory collapse phase connects a larger amplitude chevron state with a smaller amplitude chevron, which then regrows again into the larger amplitude state. The transition from this state to the blinking state appears to be again hysteretic, while the largest Rayleigh number solution ($R=1780$) appears to be periodic but with a period that is three times the basic blinking period. The only substantive difference between the results of Figs. 5 and 9 is that the parity of the chevron state involved is different. These results confirm Kolodner's experimental results and the theoretical prediction [6] that the spatio-temporal dynamics in this system should be periodic with respect to Γ with a period of π/k_c, where $k_c\approx\pi$ is the wave number obtained from linear theory. Thus, increasing the aspect ratio by one allows the system in insert an extra roll thereby changing the parity of the basic state. Our calculations indicate that the wavelength of the rolls remains remarkably uniform across the container despite the substantial changes in amplitude that occur as a result of the dynamics of these states.

The explanation of these results is the subject of the next section.

IV. THEORETICAL INTERPRETATION

In this section, we investigate the model problem

$$\dot{v}=(-\nu+cz^2)v-\delta|v|^2v, \tag{4.1}$$

$$\dot{z}=(\mu+az^2-z^4)z-|v|^2z, \tag{4.2}$$

constructed to retain the main properties of the partial differential equations. Here z refers to the amplitude of the chevron state (either even or odd) and is not to be confused with the vertical coordinate of Sec. II. We take z to be a real quantity despite the fact that the chevron states are in fact time periodic, and justify this approximation using Fig. 3, which shows that, for the parameter values considered, the chevron frequency ω_1 is high compared to the blinking frequency ω_2 or the slow frequency ω_3 associated with the repeated transients. The assumption that z is real removes one frequency from the system, and may be considered to be the result of averaging over the fast chevron frequency. Consequently, pure chevron states correspond to the solutions of the equation

$$\dot{z}=(\mu+az^2-z^4)z, \tag{4.3}$$

and we take $\mu\propto R-R_c(\Gamma)$ to be a real parameter, with the coefficient a also real. In view of the results of Sec. III, we take $a>0$ so that the primary bifurcation to chevrons is subcritical, with a saddle-node bifurcation (hereafter SN) occurring at $z^2=a/2$. The stability of these states with respect to perturbations in the form of chevrons of the same parity is therefore given by the linearization of Eq. (4.3) about the solution $z=z_0$ satisfying $\mu+az_0^2-z_0^4=0$. We denote this eigenvalue by λ. It follows that when $a<0$, this eigenvalue is always negative (stable), while if $a>0$, it is positive (unstable) on the subcritical branch and becomes negative above the saddle-node bifurcation. Note that Kolodner and Surko [5] mistakenly fit the chevron amplitude to a curve of the form $\epsilon z_0+az_0^2-z_0^4=0$.

The variable v represents perturbations transverse to the chevron invariant subspace, and is complex because these perturbations are destabilized at a secondary Hopf bifurcation, hereafter H_2. As a result, the coefficients ν, c, and δ are all complex. This Hopf bifurcation is responsible for the onset of blinking. In the model, the amplitude of the blinking is given by

$$\dot{y}=(-\nu_R+c_Rz^2)y-\delta_Ry^3 \tag{4.4}$$

and its frequency by the decoupled equation

$$\dot{\theta}=-\nu_I+c_Iz^2-\delta_Iy^2. \tag{4.5}$$

Here $v\equiv ye^{i\theta}$ and the subscripts R and I denote real and imaginary parts, respectively. In these equations the important parameter is $\nu_R\equiv\nu_R(\Gamma)>0$ and we take $c_R>0$. Because of the decoupling of θ from the equations for y and z, the resulting model is simple to analyze. Within the model, the symmetry $y\to-y$ represents evolution in time by half the blinking period so that solutions with opposite signs of y are in fact identical modulo time translation. The pure chevrons $(y,z)=(0,z_0)$ begin to blink when $z_0^2=\nu_R/c_R$ and do so with frequency $-\nu_I+c_Iz_0^2$; the resulting blinking states take the form $(y,z)=(y_0,z_0)$, provided $y_0^2>0$, $z_0^2>0$. The stability of these states is described by a quadratic dispersion relation. This relation shows that the blinking states either set in (supercritically) from the larger amplitude chevron branch (hereafter A), or from the smaller amplitude branch (hereafter B). In the former case, the chevrons acquire stability at the saddle-node bifurcation before losing it again at larger amplitude to stable blinking states. In the (y,z) variables, this bifurcation looks like a pitchfork bifurcation, although it is of course a Hopf bifurcation. In the latter case, the blinking states are initially unstable but acquire stability at a tertiary Hopf bifurcation H_3. This Hopf bifurcation is of vital importance in what follows since it introduces a third frequency ω_3 into the dynamics of the partial differential equations. As discussed further in Appendix A, its presence is a

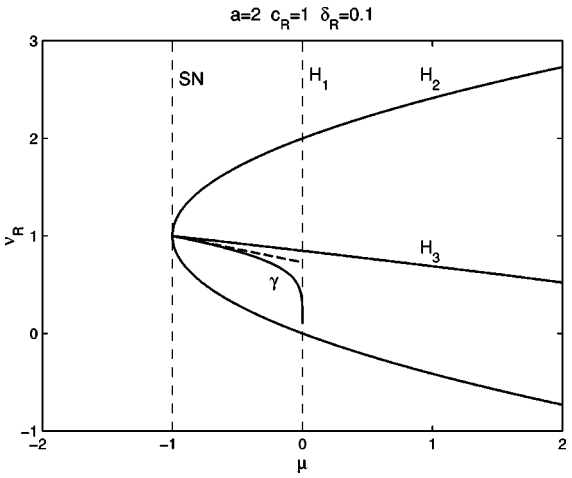

FIG. 13. Codimension-one bifurcation surfaces in the (μ,ν_R) plane for Eqs. (4.1),(4.2) with $a=2.0$, $c_R=1.0$, and $\delta_R=0.1$. H_1,: primary (Hopf) bifurcation to the chevron state $(v,z)=(0,z_0)$; SN, saddle-node bifurcation on the chevron state; H_2: (secondary) Hopf bifurcation to blinking states $(v,z)=(v_0,z_0)$; H_3: (tertiary) Hopf bifurcation from (v_0,z_0) responsible for the appearance of the three-frequency states; and γ, global bifurcation at which these states disappear. The heavy broken line represents the asymptotic result (A5).

direct consequence of the passage of the Hopf bifurcation H_2 through the saddle-node bifurcation SN on the chevron branch when $a>0$, $c_R>0$, as originally noted by Guckenheimer [22]. For a related analysis, also arising in the binary fluid context, see [23]. In the following, we present the corresponding results for the full model Eqs. (4.1) and (4.2). These are summarized in Fig. 13 for the case in which the three-frequency state created from the blinking state branch is stable. This is always the case when $c_R=1$, $\delta_R=0$, and $a>0$, and hence for sufficiently small positive values of δ_R as well. The figure shows the loci of the primary (H_1), secondary (H_2), and tertiary (H_3) Hopf bifurcations, as well as the locus of the saddle-node bifurcations (SN) on the chevron branch. It should be remembered that in the (y,z) variables only the bifurcation H_3 remains a Hopf bifurcation, with H_1 and H_2 represented by pitchfork bifurcations. In addition, the figure shows the curve γ of global bifurcations at which the limit cycle (corresponding to the three-frequency states) created at H_3 disappears by simultaneous collision with the pure chevron states *A* and *B*. The location of this line must be determined numerically. An asymptotic calculation of this curve near the codimension-two point (see Appendix A) yields the heavy broken line; this line is tangent to γ at the codimension-two point, as it must.

Figure 14 shows the bifurcation diagrams obtained by traversing the (μ,ν_R) plane in Fig. 13 along the lines $\nu_R=1.6$ and 0.7. These capture the two fundamentally different bifurcation diagrams characterizing the binary mixture. Figure 14(a) shows a small interval of subcritical but stable chevrons, followed by a supercritical pitchfork bifurcation to a state with $y_0\neq 0$ that represents a blinking state in the physical variables. In the example shown, this bifurcation occurs at $\mu<0$ so that the first stable state just above onset ($\mu=0$) is a finite amplitude blinking state. In contrast, in the case shown in Fig. 14(b) the first stable state encountered beyond $\mu=0$ is a finite amplitude periodic state that we identify with the three-frequency repeated transient state discovered by Kolodner. Figure 14(c) shows the time series corresponding to this state when $\mu=-0.21$. These oscillations represent the low frequency component of the three-frequency state, i.e., the repeated transient state with the frequencies ω_1 and ω_2 filtered out. Observe that during the growth phase of the variable *z* the variable *y* vanishes, indicating that the growing state is a pure chevron; *y* becomes nonzero only during the collapse phase, indicating that the collapse is triggered by a symmetry-breaking instability (i.e., the loss of stability of the growing chevron). Figure 15

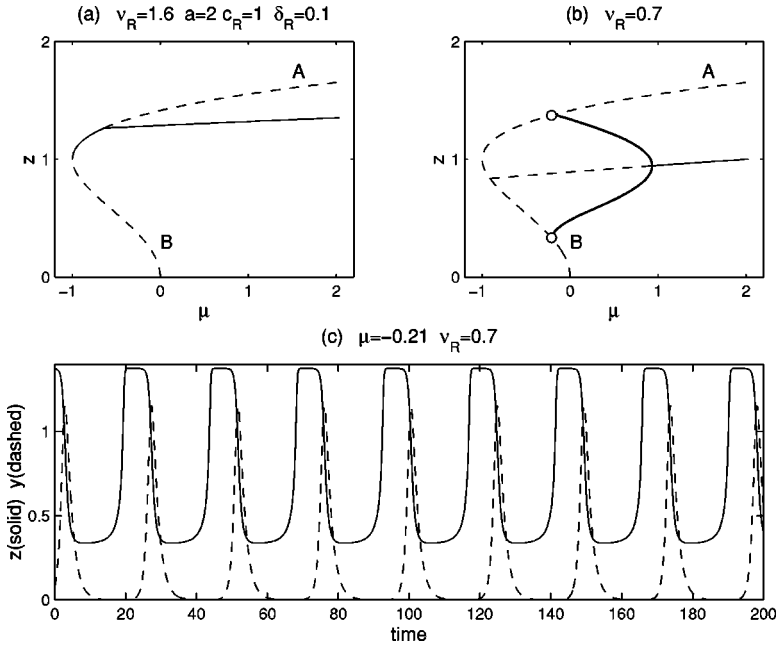

FIG. 14. (a),(b) The bifurcation diagrams along the lines $\nu_R=1.6$ and $\nu_R=0.7$ in Fig. 13. Scenario (a) corresponds to that observed in Fig. 6 for $\Gamma=16.25$, while (b) corresponds to that observed in Fig. 5 for $\Gamma=16.0$. In (b), the open circles indicate the global bifurcation with which the oscillations terminate as μ decreases, with the states *A* and *B* labeled as in the text. Solid (dashed) lines indicate stable (unstable) solutions. (c) The time series $y=|v(t)|$ (dashed) and $z(t)$ (solid) for a stable repeated transient when $\mu=-0.21$, $\nu_R=0.7$, $a=2.0$, $c_R=1.0$, and $\delta_R=0.1$.

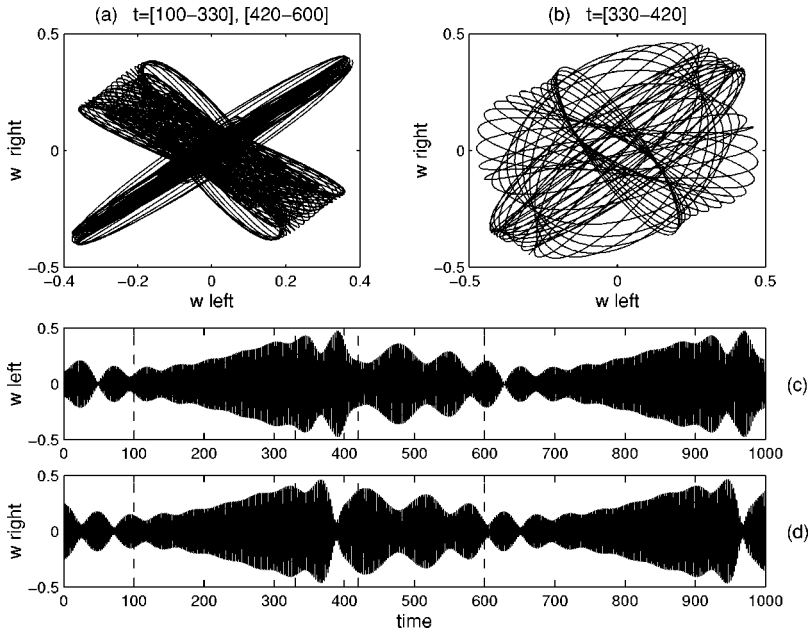

FIG. 15. Plots of $w(x=0.13\Gamma,z=0,t)$ vs $w(x=0.87\Gamma,z=0,t)$ for $\Gamma=16.0$, $R=1778.5$ during (a) the growth and the collapse phases, and (b) during the start of the collapse phase, together with the time series (c) $w(x=0.13\Gamma,z=0,t)$ and (d) $w(x=0.87\Gamma,z=0,t)$. Growing symmetric chevrons evolve along the 45° line in (a) but evolve along the orthogonal direction during the collapse phase [cf. Fig. 8(a) of [8]]. The growth, transition, and collapse phases used to construct (a),(b) are indicated by vertical dashed lines in (c),(d).

shows similar behavior obtained from the partial differential equations when $\Gamma=16.0$: during the growth phase $w(0.13\Gamma,0,t)=w(0.87\Gamma,0,t)$ indicating a growing chevron, a fact confirmed in Fig. 15(a) by the evolution of the system away from the origin along the 45° line. The collapse phase is initiated when the difference between $w(0.13\Gamma,0,t)$ and $w(0.87\Gamma,0,t)$ begins to grow and the system begins to evolve in a direction orthogonal to the 45° line, much as shown in Fig. 8(a) of Ref. [8]. With the beginning of the collapse phase, one starts to notice the onset of blinking as evidenced in the 180° phase difference between the decaying oscillations in $w(0.13\Gamma,0,t)$ and $w(0.87\Gamma,0,t)$ [Figs. 15(c) and 15(d)]. The amplitude and the period $2\pi/\omega_3$ of the limit cycle in Fig. 14(c) decreases with increasing μ, with the oscillations disappearing at H_3. As already mentioned, we interpret this transition as the transition from the repeated transient state to the (symmetric) periodic blinking state with increasing Rayleigh number (cf. Fig. 4 of [8], where H_3 is located at $\epsilon\approx 2\times 10^{-3}$, i.e., the minimum of the measured ''modulation'' period). For the model parameters, this transition is supercritical, indicating the absence of hysteresis. As μ approaches closer to the global bifurcation at $\mu=\mu^*<0$, indicated by open circles in Fig. 14(b), the time series remains similar to that shown in Fig. 14(c) but the oscillation period $2\pi/\omega_3$ becomes longer, diverging as $\ln|\mu-\mu^*|$ for $\mu\sim\mu^*$, cf. Fig. 4 of [8]. In Fig. 16, we show another case, in which the global bifurcation at μ^* occurs very close to $\mu=0$. As a result, the chevron state grows from almost zero amplitude, and so resembles more closely the repeated transient state discovered by Kolodner. In this case, there is al-

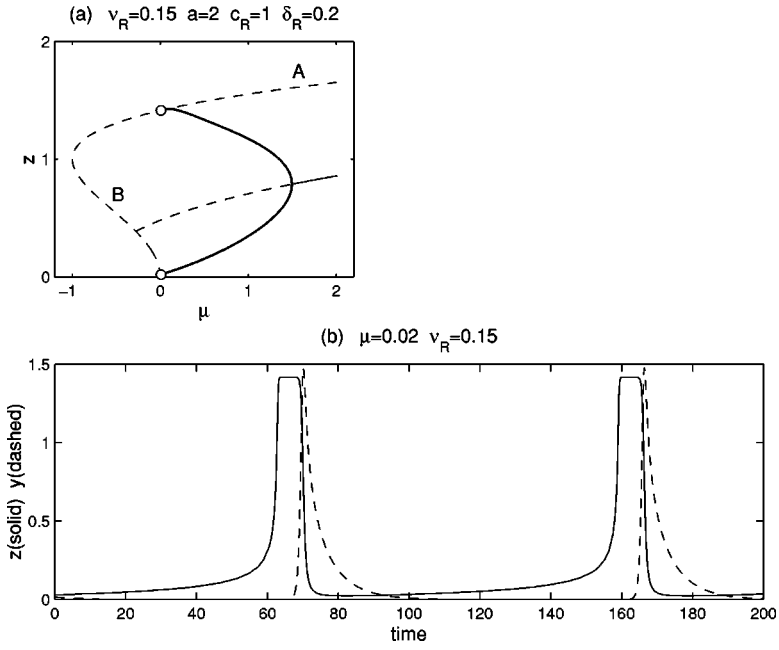

FIG. 16. (a) As for Fig. 14(b) but with $\nu_R=0.15$, $a=2.0$, $c_R=1.0$, and $\delta_R=0.2$, showing a global bifurcation very close to $\mu=0$. (b) The corresponding time series when $\mu=0.02$.

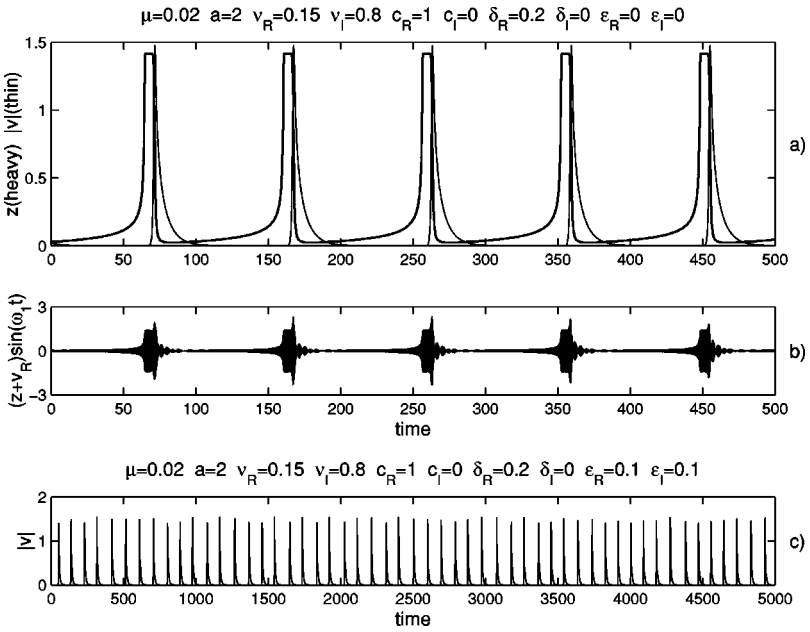

FIG. 17. (a) As for Fig. 16(b) but over a longer time interval. (b) The time series for $[z+v_R(t)]\sin\omega_1 t$ when $\nu_I=0.8$, $c_I=0$, $\delta_I=0$, and $\omega_1=20$. Note the exponential growth during the chevron phase, followed by an overshoot when the blinking instability sets in, and the ringing down during the subsequent collapse phase. The time series resembles closely that in Fig. 6(a) of Ref. [8]. (c) $|v(t)|$ for chaotic repeated transients from Eqs. (4.6), (4.7) with $\epsilon_1=0.1+0.1i$, $f_1=z^2$.

most no hysteresis between this state and the conduction state, and the system behaves *as if* the primary instability at $\mu=0$ were directly responsible for generating repeated transients. Within the model, the corresponding state has all the properties of this state observed in the experiments, except for the (apparent) absence of the oscillations during the collapse phase. In fact, if the frequencies ω_1 and $\dot{\theta}\equiv\omega_2$ determined by Eq. (4.5) are incorporated, and the quantity $[z+v_R(t)]\sin\omega_1 t\equiv[z+y(t)\cos\omega_2 t]\sin\omega_1 t$ is plotted instead of z or $|v|$, these oscillations are present [Fig. 17(b)], and their amplitude depends on the chevron amplitude z in the manner observed in the experiments. In fact, the time series shown in Fig. 17(b) displays a number of qualitative features, including the pointed overshoot at maximum as the mode v begins to grow and the ''ringing down'' due to the fact that the variable z decays more rapidly than v, that were documented by Kolodner in Fig. 6(a) of Ref. [8]. This time series is not periodic because, in general, the two (nonlinear) frequencies ω_2 and ω_3 are incommensurate.

Several remarks are in order.

(1) The coefficient δ may be zero without qualitative effect on the above scenarios. However, we have chosen $\delta_R>0$ to assure that the solutions remain bounded for all time, and to move the secondary bifurcations away from the saddle node on the primary chevron branch.

(2) The invariance of the plane $z=0$ in the model system (4.1) and (4.2) prevents the formation of a connection between the large amplitude chevron state A and the origin when $\mu>0$ (see Appendix A). Consequently, the global bifurcation with which the stable three-frequency states first appear must involve the small amplitude chevron state B, and μ^* is necessarily negative. However, there is a large range of values of ν_R for which $\mu^*\approx 0$ (see Fig. 13). Consequently, the absence of hysteresis between the conduction state and the repeated transients noted by Kolodner finds a ready explanation in Fig. 13.

(3) The model (4.1) and (4.2) lacks coupling between the blinking frequency ω_2 and the tertiary frequency ω_3 because of the built-in normal form symmetry. Since this symmetry is not exact, the coupling between these two frequencies should be restored. This leads one to consider the models

$$\dot{v}=(-\nu+cz^2)v-\delta|v|^2v+\epsilon_1 f_1(z^2)\bar{v}+\cdots, \qquad (4.6)$$

$$\dot{z}=(\mu+az^2-z^4)z-|v|^2z, \qquad (4.7)$$

where the coefficients $\epsilon_1,\ldots$ represent the coupling and are assumed to be small, cf. [24]. When this is done, one finds that the invariant sphere with A and B at its poles breaks down due to the transversal intersection of the unstable manifold of A and the stable manifold of B. These intersections occur in a heteroclinic *region* in the (μ,ν_r) plane whose width increases with ϵ_1. This region contains a countably infinite number of ''horseshoes'' and hence is associated with the presence of chaos. Note that the heteroclinic connection along the diameter BA is preserved by the perturbation $\epsilon_1\neq 0$. Figure 17(c) shows a solution of this type for $\epsilon_1=0.1+0.1i$ and $f_1=z^2$.

The model (4.1) and (4.2) described above is completely consistent with the two scenarios for generating blinking states identified in the numerical solutions of the governing partial differential equations. In the scenario observed for $\Gamma=16.25$, the blinking sets in via a supercritical Hopf bifurcation above the saddle-node bifurcation, and does so already for $\epsilon<0$ (Fig. 6). Consequently, there is only a narrow range of ϵ between this bifurcation and the saddle-node bifurcation with stable chevrons, before blinking sets in. The blinking frequency ω_2 is quite small because the chevron amplitude at which the Hopf bifurcation takes place is small [6]. In contrast, the results for $\Gamma=16.00$ (Fig. 5) and $\Gamma=17.00$ (Fig. 9) are entirely consistent with the second scenario, i.e., that the secondary Hopf bifurcation to blinking states now occurs below the saddle-node bifurcation, thereby

eliminating the stable chevrons entirely. Moreover, our results for, say, $R=1777.2$ (Fig. 5) and $R=1776.5$ (Fig. 9) are suggestive of a quasiperiodic state with three independent frequencies such as might be expected from the tertiary Hopf bifurcation H_3 on the branch of blinking states identified in the model. Indeed, our calculations are consistent with the conjecture that the bifurcations SN and H_2 on the chevron branch coincide at an aspect ratio Γ somewhere between 16.0 and 16.25. Note that the observed period associated with the third frequency is about $1000t_d$. Such low frequencies are characteristic of the scenario proposed in Fig. 13, since ω_3 vanishes at the codimension-two point $(\mu,\nu_R)=(-a^2/4, ac_R/2)$. Moreover, this scenario predicts that the corresponding modulation period should increase rapidly with decreasing ϵ, diverging when ϵ reaches the global bifurcation at $\epsilon=\epsilon^*<0$, in accord with the experimental observations (see Fig. 4 of [8]). Figure 5 also suggests that the repeated transients observed by Kolodner evolve from this three-frequency state as ϵ increases from ϵ^* towards $\epsilon\approx 0$, a suggestion that is confirmed in Fig. 9, where the three-frequency states look like Kolodner's repeated transients from the very beginning (here $\epsilon^*\approx 0$). In both cases, periodic blinking states are observed only after a (hysteretic) transition from the three-frequency repeated transients. Consequently, the branch of blinking states only acquires stability at H_3 and these states therefore blink with finite amplitude when they first appear, resulting in a longer blinking period than at H_2, typically $100t_d$ (compare Fig. 5 at $R=1779$ with Fig. 6 at $R=1776$). This period is also comparable to the period observed in the experiments. With further increase in ϵ, the blinking state appears to undergo period doubling as suggested by the time series for $R=1782$ in Fig. 5 (cf. [19,20]), and gradually becomes more and more chaotic. Indeed, the time series for $R=1780$ in Fig. 9 suggests a period-three blinking state. Available theory predicts [6] that the blinking states terminate in another global bifurcation at which a hysteretic transition to a single-frequency localized state takes place. This state consists of waves that travel under a stationary envelope attached to one or other lateral wall [6]. It is likely that the period-doubling transitions, etc., are associated with this global bifurcation. Details of this transition will be described elsewhere. Finally, the fact that we have found the repeated transients only in the vicinity of $\Gamma=16.0$ and 17.0, i.e., for aspect ratios differing by ≈ 1, is also consistent with theoretical expectation [6], and indeed the experiments as well [8].

Figures 14(b) and 16(a) lead to the following detailed interpretation of the repeated transients computed from the partial differential equations, described here as ϵ decreases from a periodic blinking state at some $\epsilon>0$. The blinking state first undergoes a (supercritical) Hopf bifurcation H_3 that introduces a third independent frequency, ω_3, into the dynamics. In fact, in both Figs. 5 and 9 this bifurcation appears to be slightly subcritical, before the new branch turns around towards smaller ϵ, but this has no bearing on what follows. The new frequency is finite and decreases with ϵ. At the same time, the amplitude of the resulting modulation increases [cf. Fig. 16(a)], a fact that may be confirmed from a careful scrutiny of Fig. 9, and the three-frequency states approach simultaneously the unstable large and small amplitude chevron states *A* and *B*. The character of the resulting repeated transient is determined by the leading eigenvalues of *A* and *B* in the chevron fixed point subspace, hereafter $-\lambda_A<0$ and $\lambda_B>0$, and the leading eigenvalues in the perpendicular direction. As shown in Appendix B, if the latter are real, $\alpha_A>0$ and $-\alpha_B<0$, say, and $\rho\equiv\alpha_B\lambda_A/\alpha_A\lambda_B>1$, the repeated transients will remain periodic and stable all the way to μ^*, where the period diverges and the global bifurcation takes place. In contrast, when $0<\rho<1$, the periodic oscillations necessarily lose stability before the global bifurcation at μ^*. Similar results obtain in the case where the leading stable symmetry-breaking eigenvalue at *B* is complex, viz. $-\alpha_B+i\omega_B$, $\alpha_B>0$, as suggested by the simulations (see Appendix B). In this case, stable periodic oscillations will persist down to μ^* if $\rho>1$, but if $0<\rho<1$ complex dynamics of Shil'nikov type will be present. In fact, Figs. 5 and 9 suggest that the leading unstable eigenvalues α_A and λ_B are also complex; this is to be expected since the bifurcations at H_1 and H_2 are in fact both Hopf bifurcations. In the following, we do not consider the resulting complications further.

When λ_B is real, a trajectory escaping from *B* describes an exponentially growing chevron state. This growth phase, including the states *A* and *B*, is clearly visible in the time series for $R=1776.2$ (Fig. 9). When the growing chevron reaches the vicinity of *A* it becomes unstable to symmetry-breaking oscillations, which take it back near *B*. This is the collapse phase of the repeated transient state [compare Figs. 14(c) and 16(b) with Fig. 15]. The frequency of the decaying oscillations observed in the time series in Figs. 15(c) and 15(d) is given by ω_B. This frequency will in general be of the same order as the blinking frequency associated with the branch of blinking states when these bifurcate from the small amplitude chevron *B*, but quite different from (and in general larger than) the blinking frequency of the *stable* blinking states beyond H_3, cf. [8]. This observation explains the coincidence of the period of the blinking states and of the oscillations during the collapse phase of the repeated transient also noted by Kolodner. Note also that since the repeated transient state visits the states *A* and *B* whose amplitude decreases (respectively, increases) as ϵ becomes more negative the modulation amplitude along the branch of three-frequency states should decrease towards the end of the branch. This is seen quite dramatically in Fig. 5. Moreover, since α_B decreases as ϵ decreases (it passes through zero at H_2, i.e., at $\epsilon=\epsilon_2$) the collapse becomes slower and slower, as also seen in Fig. 5, but is still finite when the three-frequency states disappear in the global bifurcation at ϵ^* (since $\epsilon_2<\epsilon^*<0$) and the system makes a hysteretic transition to the conduction state. The fact that α_B decreases with ϵ makes it likely that the Shil'nikov condition $0<\rho<1$ holds at ϵ^* (see Appendix B), resulting in *chaotic* repeated transients prior to their disappearance [20]. This possibility apparently does not occur in Figs. 5 and 9 but may occur in the experiments. In any case, even longer time series would be required to test this prediction. Note that since $\lambda_B\propto|\epsilon|$ only periodic repeated transients will occur if $\epsilon^*\approx 0$, although even in this case, there may be a few bifurcation

bubbles with chaotic dynamics, as in Ref. [25]. In [8], Kolodner notes that the growth phase of the repeated transient is inversely proportional to ϵ, in accord with the above scenario. It is of interest that the repeated transients are most likely to be chaotic just prior to their extinction, as ϵ decreases.

We note, finally, that despite the fact that the repeated transients are three-frequency states they are not necessarily structurally unstable. In the model, this is because we have averaged out the chevron frequency ω_1. However, even if we had not done so, genuinely three-frequency states may be observed in open parameter regions [26] despite the Ruelle-Takens theorem [27].

V. DISCUSSION

In this paper, we have used direct numerical simulations of the partial differential equations governing binary fluid convection in a two-dimensional container with realistic boundary conditions applied on all four boundaries to describe in detail the behavior of the system near onset of overstability. These calculations revealed a complex sequence of transitions among states we have called chevrons and two other states called blinking and repeated transients as the aspect ratio or the applied Rayleigh number varies. We have seen that:

(i) The primary bifurcation to convection is subcritical, in agreement with the prediction for *standing waves* in a horizontally unbounded layer [10,17]. As a result, for some aspect ratios, stable chevrons may be present, but are most likely observed for negative values of ϵ.

(ii) For many (though not most) aspect ratios, the first nontrivial state of the system is a three-frequency repeated transient state. The transition to this state is hysteretic since $\epsilon^* < 0$ but for many parameter values ϵ^* is so close to zero as to make the detection of hysteresis highly unlikely. Indeed, in some experiments no hysteresis was found [5]. The three-frequency states appear via a global bifurcation and acquire the characteristic behavior associated with repeated transients only as ϵ increases. Consequently the modulation period $2\pi/\omega_3$ is infinite when the repeated transients first appear, but drops rapidly with increasing ϵ, as observed in Fig. 4 of [8]. When the condition $\rho < 1$ on the eigenvalues at *A* and *B* holds (see Appendix B), the resulting repeated transients are expected to be chaotic. These states persist only over a narrow interval of ϵ close to onset, of order 10^{-3} (see Fig. 8), which compares well with the range 2×10^{-3} given by Kolodner for $\Gamma = 16.75$ [8], and give way to large amplitude blinking states in a (slightly) hysteretic transition when $\epsilon \approx 10^{-3}$. Our calculations suggest that dispersive effects are not of fundamental importance in this behavior (in contrast to Kolodner's conjecture), but that the primary chevron state must bifurcate subcritically. In particular, we have been unable to identify any fundamental role of the local wavenumber changes observed in the experiments.

(iii) Stable small amplitude blinking states set in when stable chevrons lose stability at a secondary Hopf bifurcation.

(iv) Stable large amplitude blinking states set in via a (typically hysteretic) bifurcation from the repeated transient state. This bifurcation eliminates the slowest frequency from the time trace.

(v) In the experiments, the blinking states become irregular with increasing ϵ and the blinking period gradually increases, until an abrupt transition to a localized traveling wave state attached to one boundary (or to steady overturning convection) takes place. The observed chaotic blinking is likely associated with the global bifurcation studied in [6,20], and will be described elsewhere.

(vi) Although the chaotic asymmetric blinking states are easily confused with the repeated transients because of their somewhat similar appearance, cf. [8], their origin is undoubtedly quite different and most likely occurs via spatial symmetry breaking followed by period doubling. This difference is seen clearly in the simulations, and is captured by the model system proposed in Sec. IV.

(vii) Regular blinking states are observed near onset only for aspect ratios differing roughly by unity, as in the experiments. Our simulations suggest (Fig. 3) that these special aspect ratios are in fact nothing but the mode interaction points (compare Fig. 2(a) with Fig. 3). The location of these points depends quite sensitively on the system parameters and in particular on the additional dissipation due to the neglected no-slip walls in the third (transverse) direction. Consequently, differences between the experimental results and our calculations may be primarily due to differences in the location of these points. For example, Kolodner finds that blinking states persist down to small amplitudes for $\Gamma = 16.63$ and 17.63 when the (dimensionless) width $\Gamma_y = 3.0$, and for $\Gamma = 16.25$ and 17.25 when $\Gamma_y = 4.9$. In contrast, our strictly two-dimensional calculations ($\Gamma_y = \infty$) show that blinking states are most easily found near $\Gamma \approx 16.8$. In contrast to the experiments [8], we do not find that repeated transients predominate at all aspect ratios away from the mode interaction points. For example, at $\Gamma \approx 16.25$, we found subcritical stable chevrons that bifurcate into blinking states with increasing ϵ (Fig. 6).

(viii) The behavior exhibited by the partial differential equations is fundamentally low-dimensional even though the aspect ratio is quite large. This is because the dynamics of interest occurs in a small range of ϵ near onset, $|\epsilon| \ll \Gamma^{-2}$.

(ix) The numerical simulations support much of the theory put forward by Dangelmayr and co-workers [6] (see also [19]) as to the origin of the different types of states, and provide essential information supporting the interpretation of the repeated transients as a three-frequency state. The simulations also confirm the significance of the parameter Γ mod π/k_c proposed in [6] and confirmed so dramatically in Kolodner's experiments [8]. This parameter reflects the fact that when Γ changes by π/k_c, where k_c is the "wave number" of the waves, an additional roll fits into the container, thereby changing the parity of the most unstable state. Detailed calculations [16] indicate that the wave number at onset is in fact remarkably uniform across the cell (cf. [8]), despite the variation in amplitude, and that $k_c \approx \pi$. Thus, when the neutral curves of both modes cross, the system feels comfortable with both, and oscillates regularly even in

the nonlinear regime. This is not so for other aspect ratios for which one or another mode is preferred: when the preferred mode loses stability at finite amplitude to a symmetry-breaking perturbation the competing state does not fit well into the container and the system oscillates irregularly.

These results and the accompanying interpretation account quantitatively for almost all of the experimental observations of Kolodner [8], and put forward a dynamical systems explanation for the diversity of the observed states and their properties. The numerical simulations proved essential, first, to reproduce quantitatively the periods of the observed states and their spatio-temporal character, in order to confirm that the restriction to two dimensions is not fatal, and second, to verify certain aspects of the dynamical systems description that could not be identified in the published experimental data. It is our view that the remaining quantitative discrepancies may all be attributed to the sensitive dependence of the mode interaction point on the width of the container, because of its effect on dissipative processes in the cell.

The results reported here indicate that for sufficiently small $|\epsilon|$ sidewalls exert a critical influence on the dynamics of the system. This is to be expected since for such ϵ the behavior of the system is dominated by one (or at most two) unstable modes of the system, whose spatial structure is determined by the lateral boundary conditions. Order of magnitude estimates [6,28] suggest that this will be the case whenever $|\epsilon|\Gamma^2 \lesssim 1$, i.e., with increasing $|\epsilon|$ the sidewall influence becomes smaller, and indeed one may reach the situation in which the collapse described by the subcritical Ginzburg-Landau equation on an unbounded domain becomes a more and more appropriate description of the dynamics [29]. The experiments of Kaplan *et al.* [29] suggest that this is in fact so once $|\epsilon|\Gamma^2 \gtrsim 10$. The results of Ref. [30], performed for slightly larger $|S|$ and subcritical values of ϵ, may likewise be interpreted as showing that $|\epsilon|\Gamma^2 \approx 5$ describes the transition between these two regimes. However, the simulations reported here all satisfy the condition $|\epsilon|\Gamma^2 \lesssim 1$, and hence are always dominated by the sidewalls.

We conclude with a remark about modeling systems of this type using amplitude equations. Such equations apply rigorously near the mode crossing point, and describe the interaction of the two competing chevrons. In a finite domain, one cannot derive coupled equations for the amplitudes of left- and right-traveling waves, since such waves are not eigenstates of the linear problem. In the following, we therefore let z_+ and z_- denote the (complex) amplitudes of the even and odd chevron eigenfunctions (Fig. 1). Owing to the reflection symmetry $x \to -x$, $(\psi, \theta, \eta) \to (-\psi, \theta, \eta)$ of the original system (2.1)–(2.3) these equations must commute with the operation

$$(z_+, z_-) \to (z_+, -z_-). \tag{5.1}$$

Since the frequencies of the two competing modes are within about 10% of one another, we include two formally nonresonant cubic terms in the amplitude equations and write these in the form, cf. [31,32,16],

$$\dot{z}_+ = (\mu_+ + i\omega_+) z_+ + A_+ |z_+|^2 z_+ + B_+ |z_-|^2 z_+ + C_+ \overline{z}_+ z_-^2, \tag{5.2a}$$

$$\dot{z}_- = (\mu_- + i\omega_-) z_- + A_- |z_-|^2 z_- + B_- |z_+|^2 z_- + C_- \overline{z}_- z_+^2, \tag{5.2b}$$

where $A_\pm$, $B_\pm$, $C_\pm$ are complex $O(1)$ coefficients, and $\mu_\pm$, $\omega_\pm$ denote the growth rates and frequencies of the two modes at a particular point in the (R,Γ) plane. Renardy [28] shows that equations of this form may also be derived, via center manifold reduction, from a pair of coupled complex Ginzburg-Landau equations with generic boundary conditions. Note that as $|\omega_+ - \omega_-|$ becomes larger and larger, the $C_\pm$ terms become less and less important.

The model put forward in Sec. IV suggests that Eqs. (5.2) are not adequate for describing the dynamics of binary fluid convection in the parameter regime considered. This is because to capture the repeated transients, the primary bifurcation to the chevron state must be subcritical, i.e., $A_{\pm R} > 0$, and in this case, the amplitude equations must be determined to higher order. It is for this reason that the mechanism for generating bursts put forward by Moehlis and Knobloch [33] does not operate for these parameter values, and is presumably also the reason why the present system exhibits repeated transients, as opposed to the type of bursting observed by Sullivan and Ahlers [34] in He^3-He^4 mixtures. The same argument applies to the derivation of coupled complex Ginzburg-Landau equations for this system. It is for this reason that we have not pursued this type of description further.

ACKNOWLEDGMENTS

We thank Vivien Kirk for helpful discussions. This work was supported by Fulbright US-Spain Science and Technology Joint Research Grant No. 99231 and by DGICYT under Grant No. PB97-0683. Additional support from National Science Foundation Grant No. DMS-0072444 is gratefully acknowledged. Computer time was provided by CEPBA.

APPENDIX A: THE GLOBAL BIFURCATION AT $\mu = \mu^*$

In this Appendix, we summarize the results of analyzing the interaction of the saddle-node bifurcation on the chevron branch with the pitchfork bifurcation to the blinking state, and then explore the location of the global bifurcation identified there for parameter values away from this codimension-two point. The analysis is done within the system (4.1) and (4.2), written in real variables. For convenience, the subscripts on ν_R, c_R, and δ_R are dropped.

1. The saddle-node–pitchfork interaction

Within the system (4.1) and (4.2) the saddle-node bifurcation occurs at $\mu = -a^2/4$. The pitchfork coincides with this bifurcation when $\nu = ac/2$. Moving the saddle-node am-

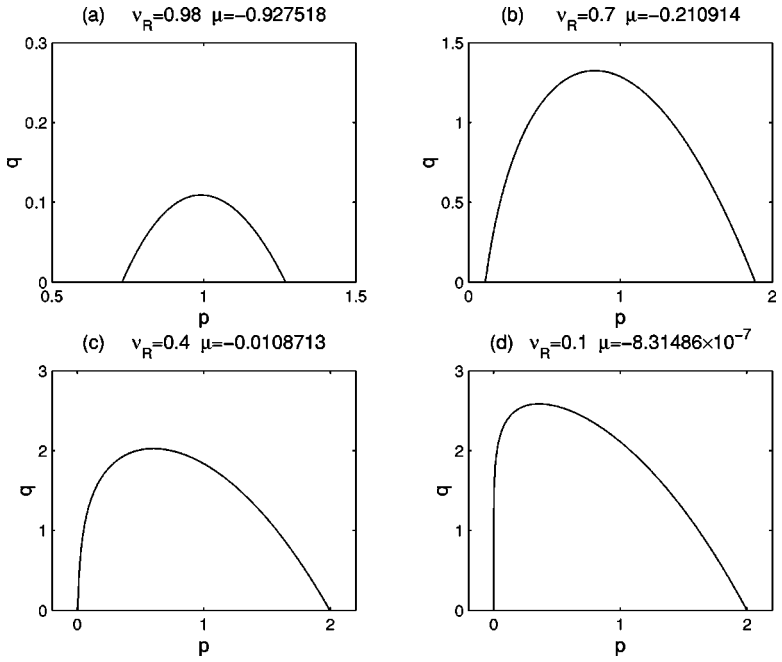

FIG. 18. Solutions of Eqs. (A8), (A9) reformulated as a nonlinear eigenvalue problem of the form (A12) for different values of $\nu \equiv \nu_R$ and $a=2.0$, $c=1.0$, $\delta=0.1$. (a) $\nu=0.98$, (b) $\nu=0.7$, (c) $\nu=0.4$, and (d) $\nu=0.1$. The eigenvalues μ^* are all negative. Note that $\mu^* \approx -10^{-2}$ when $\nu=0.4$, and $\approx -10^{-6}$ when $\nu=0.1$.

plitude $z_{SN}=\sqrt{a/2}$ to the origin, and scaling the resulting equations appropriately (cf. [35]), we can rewrite Eqs. (4.1) and (4.2) in the form

$$\dot{r}=\frac{c}{a}rz+\epsilon r\left(-\nu_1+\frac{c}{2a^3}z^2-\frac{\delta}{a^2}r^2\right), \tag{A1}$$

$$\dot{z}=\mu_1 a^2-z^2-r^2+\epsilon z\left(\mu_1-\frac{r^2}{a^2}-\frac{2}{a^2}z^2\right). \tag{A2}$$

To obtain these equations, we have written $\mu=-(a^2/4)+\epsilon^2\mu_1$ and $\nu=(ac/2)+\epsilon^2\nu_1$. The resulting equations constitute case III in the classification of Ref. [35]. The limit $\epsilon=0$ is integrable with the integral

$$F(r,z)=r^{2a/c}\left[\mu_1 a^2-\frac{a}{a+c}r^2-z^2\right]. \tag{A3}$$

If we define a new time variable τ using $dt=r^{(2a/c)-1}d\tau$ we obtain on the right-hand side a vector field that is at leading order divergence-free. It is therefore the divergence of the $O(\epsilon)$ terms that determines the surviving periodic orbits

$$\int\int r^{(2a/c)-1}\left[\mu_1-\frac{2a}{c}\nu_1-\frac{1}{a^2}\left(1+2\delta+\frac{2a}{c}\delta\right)r^2-\frac{5}{a^2}z^2\right]drdz=0, \tag{A4}$$

where the integral is to be taken over the interior of the domain $F(r,z)=K$. For example, for the values $a=2$, $c=1$ used to generate Fig. 14(b) the heteroclinic loop corresponding to $K=0$ is located along the curve

$$\nu_1=-\frac{1}{7}\mu_1[1+9\delta]. \tag{A5}$$

As shown in Fig. 13, this result (dashed line) is tangent at the codimension-two point to the locus of global bifurcations computed numerically, and is consistent with the bifurcation diagram in Fig. 14(b) since the tertiary Hopf bifurcation is present only for $\nu<ac/2$ (i.e., $\nu_1<0$), and the termination point of the resulting oscillations must lie in $\mu>-a^2/4$ (i.e., $\mu_1>0$).

It is of interest to examine the effects of breaking the S^1 invariance of the normal form as discussed in Sec. IV. To this end, we consider the system

$$\dot{v}=(\lambda+i\omega)v+\frac{c}{a}vz+\epsilon_2|v|^2z, \tag{A6}$$

$$\dot{z}=\mu-z^2-|v|^2+\epsilon_1 z^3. \tag{A7}$$

In this model, we have retained just one of the higher-order terms ($\epsilon_1\neq 0$), and use $\epsilon_2\neq 0$ to break the S^1 invariance. The resulting equations have been investigated by Kirk [24]. When $\epsilon_2=0$ and $\epsilon_1<0$ the oscillations created at H_3 are stable and disappear in a global bifurcation involving both the larger (A: $z>0$) and smaller (B: $z<0$) amplitude chevrons, i.e., in a heteroclinic bifurcation. The bifurcation diagram of Fig. 14(b) corresponds to Kirk's Fig. 2 traversed along the line $\mu+\sigma\lambda=\tau$, where $\sigma,\tau>0$. When $\epsilon_2\neq 0$, Kirk shows that the heteroclinic connection splits into a *heteroclinic region* in the (μ) plane inside of which the unstable manifold of A intersects the stable manifold of B in a structurally stable way. Consequently, this region contains a countably infinite number of horseshoes (but no homoclinic orbits). Moreover, Kirk identifies a sequence of resonance tongues in the (μ) plane containing pairs of frequency-locked orbits with frequencies in the ratio P/Q, and shows

that the tongue boundaries accumulate on the boundaries of the heteroclinic region as $Q\to\infty$. Here Q denotes the number of times in a period the orbit winds around the z axis (i.e., the number of times it follows the primary periodic orbit $(v,z)=(r_0\exp i\omega t, z_0)$, with (r_0,z_0) constant), while P is the number of times it twists around this orbit. Thus the heteroclinic region contains at least two heteroclinic orbits, as well as a variety of periodic orbits obtained by period doubling of the different P/Q orbits. Moreover, the global bifurcation responsible for the heteroclinic region always either precedes *or* coincides with that at which the lower fixed point B is annihilated in a saddle-node bifurcation with the extra fixed point introduced by the cubic term when $\epsilon_1<0$ ([36] and Fig. 3 of Ref. [24]). Figure 13 indicates that this is the case here as well, with the bifurcation at $\mu=0$ playing the role of the second saddle-node bifurcation in Kirk's problem.

2. The nonlinear eigenvalue problem

Based on Figs. 13 and 18, we have argued that within the two-dimensional model (4.1) and (4.2) the oscillations must terminate in a heteroclinic bifurcation at $\mu^*<0$, i.e., that the transition to the repeated transient state must always be hysteretic. However, the discussion of Appendix A 1 suggests that in some cases μ^* could vanish, eliminating all trace of hysteresis. This issue remains unresolved. To appreciate the difficulties, it is helpful to rewrite the equations in the form

$$\dot{p}=2p(\mu+ap-q-p^2), \tag{A8}$$

$$\dot{q}=2q(-\nu+c_Rp-\delta_Rq), \tag{A9}$$

where $p\equiv z^2$ and $q\equiv y^2$. A further rescaling, using a small parameter $\gamma\ll 1$, of the form

$$(p,q)\to\gamma(p/a,q/\delta_R),\quad (\mu,\nu)\to\gamma(\mu,\nu),$$

allows us to write this system in the equivalent form

$$p_\tau=p(\mu+p+bq-\gamma p^2), \tag{A10}$$

$$q_\tau=q(-\nu+cp-q), \tag{A11}$$

where $\tau=2\gamma t$, $b=-1/\delta_R<0$, $c=c_R/a>0$, and a factor of a^2 has been absorbed in the definition of γ. As a result, the existence of a connection between the points $(p^+,0)$ and $(0,0)$ amounts to the existence of a solution $\mu=\mu^*\geqslant 0$ of the nonlinear eigenvalue problem

$$\frac{dq}{dp}=\frac{q}{p}\frac{(-\nu+cp-q)}{(\mu+p+bq-\gamma p^2)}, \tag{A12}$$

subject to the conditions that $q(0)=0$, $q(p^+)=0$. We expect the solution $q(p)$ to be single-valued. Typical solutions of this problem for different values of ν are shown in Fig. 18.

3. The case $\gamma=0$

In the limit $\gamma\to 0$, the large amplitude fixed point moves off to infinity and the system (A10) and (A11) becomes

$$p_\tau=p(\mu+p+bq), \tag{A13}$$

$$q_\tau=q(-\nu+cp-q). \tag{A14}$$

When $\mu>0$, $\nu>0$, there are then no fixed points on either of the axes, except for that at the origin (0,0). The resulting equations may be solved using matched asymptotic expansions, valid even when the limit cycle comes close to the origin and hence is of large size.

In the regime $p\ll 1$, $p\ll q$, we approximate Eqs. (A13) and (A14) by

$$p_\tau=p(\mu+bq), \tag{A15}$$

$$q_\tau=q(-\nu-q), \tag{A16}$$

with solution curves given by

$$p=K_1q^{-\mu/\nu}(\nu+q)^{(\mu-b\nu)/\nu}. \tag{A17}$$

In the regime $q\ll 1$, $q\ll p$, we approximate Eqs. (A13) and (A14) by

$$p_\tau=p(\mu+p), \tag{A18}$$

$$q_\tau=q(-\nu+cp), \tag{A19}$$

with solution curves given by

$$q=K_2p^{-\nu/\mu}(\mu+p)^{(\nu+c\mu)/\mu}. \tag{A20}$$

Since these have to agree near the origin, i.e., for $p\ll 1$, $q\ll 1$, we conclude that

$$K_2^\mu\mu^{\nu+c\mu}=K_1^\nu\nu^{\mu-b\nu}. \tag{A21}$$

The above solutions may be matched to the solution of the equations

$$p_\tau=p(p+bq), \tag{A22}$$

$$q_\tau=q(cp-q), \tag{A23}$$

obtained from Eqs. (A13) and (A14) under the assumption $p\gg 1$, $q\gg 1$. This equation has solution curves given by

$$p^c=K^{c-1}q\left|\beta-\frac{q}{p}\right|^{-(1+bc)/(1+b)}, \tag{A24}$$

where $\beta=(c-1)/(b+1)$. Matching to the solution for $p\ll 1$, $p\ll q$ yields

$$K_1=K^{b+1}. \tag{A25}$$

Matching to the solution for $q\ll 1$, $q\ll p$ yields

$$K_2=K^{1-c}|\beta|^{(1+bc)/(1+b)}. \tag{A26}$$

On substitution of these expressions into the relation (A21) we obtain finally

$$K=|\beta|^{(1+bc)/(1+b)\mu\delta}\mu^{\delta(\nu+c\mu)}\nu^{\delta(-\mu+b\nu)}, \tag{A27}$$

where $\delta=[(1+b)\nu-\mu(1-c)]^{-1}$.

The above calculation shows that for $\mu>0$ there is always a finite amplitude limit cycle. This limit cycle is unique, in the sense that there is a single solution for each pair (μ,ν). The only exception arises in the limit $\delta\to\infty$. This limit will be recognized as the integrable limit and indeed in this case there is a one-parameter family of solutions, one for each $K>0$. When $\delta\neq 0$ the solution near the origin (0,0) is given by

$$p^{\nu}q^{\mu}=|\beta|^{\delta(1+bc)\mu\nu}\mu^{\delta\nu(1+b)(\nu+c\mu)}\nu^{\delta\mu(1-c)(-\mu+b\nu)}. \tag{A28}$$

This expression may be used to obtain the closest distance to the origin (0,0) as a function, for example, of μ. Moreover, one may check that there is always a solution to the equation $q_{\tau}=0$, $q\neq 0$, so that the solutions cannot escape to infinity in the q direction, and likewise for the p direction. These conclusions continue to hold when $\mu=0$. Thus, at least in the limit $\gamma\to 0$, the global bifurcation must occur at $\mu^{*}<0$. Note, finally, that Eq. (A24) implies that depending on the sign of $(1+bc)/(1+b)$ either p or q must diverge along the line $q=\beta p$, and hence that both do so. Since $c>0$ this ''connection to infinity'' requires that $\beta>0$. In a closely related problem, Tobias *et al.* [37] show that such a connection may occur once μ reaches a finite value.

APPENDIX B: STABILITY OF THE LIMIT CYCLE NEAR ϵ^{*}

The stability of the limit cycle identified in both the model and in the partial differential equations (PDEs) near the global bifurcation may be determined using appropriately constructed return maps. It turns out that although the model captures the essence of all the important transitions observed in the PDEs, it oversimplifies the situation near this bifurcation. This is of course because the model cannot describe complex dynamics. To appreciate the difference between the model and the PDEs, we treat first the model, and then compare the results with the corresponding ones for the PDEs.

We let $\{\alpha,\lambda\}$ be the eigenvalues of the chevrons $(0,z_0)$ in the symmetry-breaking and the symmetry-preserving directions, respectively. In the model, these eigenvalues are necessarily real and are easily computed: $\{\alpha,\lambda\}=\{-\nu_R+c_R z_0^2, 2(a-2z_0^2)z_0^2\}$, where $z_0=z_A$ or z_B. Hereafter, we refer to these eigenvalues as $\{\alpha_A,-\lambda_A\}$, and $\{-\alpha_B,\ \lambda_B\}$, respectively, with $\alpha_{A,B}>0$, $\lambda_{A,B}>0$. Explicit expressions are readily obtained. For example,

$$\lambda_B=\sqrt{a^2+4\mu}(a-\sqrt{a^2+4\mu})\approx -2\mu$$

when $|\mu|\ll a$. In the PDEs, the role of these eigenvalues is taken by the *leading* symmetry-breaking and the *leading* symmetry-preserving eigenvalues, respectively; the leading eigenvalues are those in each category with the *smallest* real part (in absolute value). In the present paper we do not compute these eigenvalues from the pdes, although some indication of their character and magnitude can be gleaned from the time series for the repeated transients (Figs. 5 and 9).

We identify ϵ-neighborhoods of A and B and construct surfaces of section at $y=\epsilon$ (labeled Σ_0 at B and Σ_3 at A), and $z-z_B=\epsilon$ (labeled Σ_1) and $z-z_A=-\epsilon$ (labeled Σ_2). See Fig. 19. When ϵ is small enough, the flow near B can be approximated by the linear flow

$$\dot{y}=-\alpha_B y,\quad \dot{\zeta}=\lambda_B\zeta, \tag{B1}$$

where $\zeta=z-z_B>0$. The map $T_{01}:\Sigma_0\to\Sigma_1$ that takes points of the form $(\epsilon,\zeta_0)\in\Sigma_0$ to $(y_1,\epsilon)\in\Sigma_1$ then takes the form

$$y_1=\epsilon(\zeta_0/\epsilon)^{\alpha_B/\lambda_B}. \tag{B2}$$

Since trajectories starting near $(0,\epsilon)\in\Sigma_1$ follow the structurally stable heteroclinic connection connecting B to A (i.e., $y=0$), the linearized map $T_{12}:\Sigma_1\to\Sigma_2$ takes the form

$$y_2=a y_1, \tag{B3}$$

where $a>0$ is a constant. Near A, the linear flow takes the form

$$\dot{y}=\alpha_A y,\quad \dot{\zeta}=-\lambda_A\zeta, \tag{B4}$$

where $\zeta=z-z_A<0$. A similar calculation now gives the map $T_{23}:\Sigma_2\to\Sigma_3$:

$$\zeta_3=-\epsilon(y_2/\epsilon)^{\lambda_A/\alpha_A}. \tag{B5}$$

Finally, the map $T_{30}:\Sigma_3\to\Sigma_0$ is given by linearizing the flow around the near heteroclinic trajectory $A\to B$:

$$\zeta_0=b\zeta_3+\sigma, \tag{B6}$$

where $b<0$ is another constant, and $\sigma\propto\mu-\mu^{*}$. Thus, when $\sigma=0$ the point $(\epsilon,0)\in\Sigma_3$ is mapped into $(\epsilon,0)\in\Sigma_0$, i.e., there is a heteroclinic connection from A to B, and hence a heteroclinic cycle of the form $B\to A\to B$. This is exactly what happens at μ^{*}.

Using the four maps just defined we may now compute the return map $T_{00}:\Sigma_0\to\Sigma_0$ taking $(\epsilon,\zeta)\in\Sigma_0$ to $(\epsilon,\zeta')\in\Sigma_0$ once around the heteroclinic cycle. The result is

$$\zeta'=c\zeta^{\rho}+\sigma,\quad \rho\equiv\frac{\alpha_B\lambda_A}{\alpha_A\lambda_B}>0, \tag{B7}$$

where $c>0$. Note that the exponent ρ is the ratio of the product of the two stable eigenvalues to the product of the two unstable eigenvalues. This equation has a fixed point given by the solution of the equation

$$\zeta-\sigma=c\zeta^{\rho}. \tag{B8}$$

A fixed point with $\zeta\ll 1$ corresponds to a periodic trajectory in the original system lying close to the heteroclinic cycle $\zeta=0$ at $\sigma=0$. Its stability is determined by the slope of the right side of Eq. (B7) at the fixed point. Thus, when $\rho>1$ such a fixed point exists only for $\sigma>0$, i.e., for $\mu>\mu^{*}$, and it is then stable. In contrast, when $0<\rho<1$ the fixed point exists only for $\sigma<0$, i.e., for $\mu<\mu^{*}$, and is then unstable. The former case describes a limit cycle that approaches the global bifurcation from above without loss of stability, while

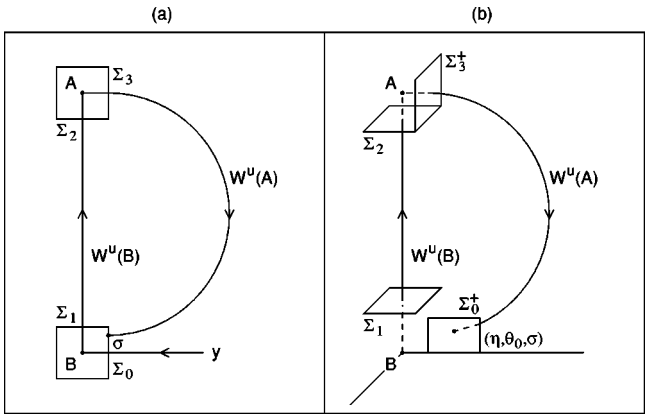

FIG. 19. Sketch of the surfaces of section used to construct the Poincaré return map near the global bifurcation for (a) the model, and (b) the PDEs. In (a), all the eigenvalues are real while in (b) the leading stable eigenvalue of B is complex.

in the latter case, the branch of stable oscillations overshoots μ^*, and turns around at a saddle-node bifurcation before approaching μ^* from below.

It is important to observe that in the model we may treat the unstable directions $\pm y$ independently. However, as already mentioned, the fact that the bifurcation at H_2 is in fact a Hopf bifurcation relates these two directions, and implies that trajectories starting near B can arrive at A from either direction. To apply the present approach to the PDEs it is necessary therefore to generalize it to the case where the leading stable eigenvalue of the steady state B is a member of a complex conjugate pair, $-\alpha_B \pm i\omega_B$, say. In the following, we retain the notation $\{\alpha_A, -\lambda_A\}$ for the leading eigenvalues of the large amplitude chevrons in the symmetry-breaking and the symmetry-preserving directions, respectively, with λ_B the unstable eigenvalue at B. Since the stable manifold of B is now two-dimensional, we use polar coordinates to describe the linearized flow

$$\dot{r} = -\alpha_B r, \quad \dot{\theta} = \omega_B, \quad \dot{\zeta} = \lambda_B \zeta. \tag{B9}$$

For Σ_0 we choose a part of the plane $\theta = \theta_0$ around one of the points $(r,\zeta) = (\eta,\sigma)$, where the unstable manifold of A intersects it. Since the symmetry $y \to -y$ implies that there are two such intersections, we take $\Sigma_0 = \Sigma_0^- \cup \Sigma_0^+$, with Σ_0^+ chosen if the intersection is with $\theta = \theta_0$ and Σ_0^- if it is with $\theta = \theta_0 + \pi$. Note that η is a small but finite quantity, while σ takes values near $\sigma = 0$. The map $T_{01}: \Sigma_0 \to \Sigma_1$ then takes the form

$$r_1 = r_0(\zeta_0/\epsilon)^{\alpha_B/\lambda_B}, \quad \theta_1 = -\frac{\omega_B}{\lambda_B}\ln(\zeta_0/\epsilon) + \theta_0, \tag{B10}$$

while the map $T_{12}: \Sigma_1 \to \Sigma_2$ is given by

$$x_2 = r_1 \cos(\theta_1 + \psi), \quad y_2 = r_1 \cos(\theta_1 + \phi). \tag{B11}$$

What happens next depends on the sign of the quantity y_2, which determines whether the trajectory will exit the neighborhood of A along through Σ_3^+ or Σ_3^- (Fig. 19). This map is given by Eq. (B5), with y_2 replaced by $|y_2|$. The remaining map, $T_{30}^{\pm}: \Sigma_3^{\pm} \to \Sigma_0^{\pm}$, is given by

$$r_0 = \eta + a|x_3| + b\zeta_3, \quad \zeta_0 = \sigma + c|x_3| + d\zeta_3, \tag{B12}$$

where $a, \ldots$ are constants, $\sigma \propto \epsilon - \epsilon^*$, and x_3 represents the x coordinate in the plane Σ_3 in the direction of the leading stable symmetry-breaking eigenvector. If this eigenvalue is more stable than λ_A this map may be simplified by noting that at leading order $r_0 \approx \eta$, so that Eqs. (B12) may be approximated by

$$\zeta' = \sigma + d\zeta_3. \tag{B13}$$

The final return map then takes the form

$$\zeta' = \sigma + e\zeta^{\rho}\cos^{\delta_A}\left(\frac{\omega_B}{\lambda_B}\ln\zeta + \Phi\right),$$
$$\rho \equiv \alpha_B\lambda_A\alpha_A\lambda_B > 0,$$
$$\delta_A \equiv \lambda_A/\alpha_A > 0, \tag{B14}$$

where $e > 0$ and Φ are constants, and is defined for $\cos[(\omega_B/\lambda_B)\ln\zeta + \Phi] > 0$ only. Fixed points of this map represent asymmetric periodic orbits, while symmetric orbits are found as fixed points of the other ''half'' of this map

$$\zeta' = \sigma + e\zeta^{\rho}\cos^{\delta_A}\left(\frac{\omega_B}{\lambda_B}\ln\zeta + \Phi + \pi\right), \tag{B15}$$

where, once again, the cosine must be positive. The resulting map (cf. [38]), has properties similar to the standard Shil'nikov map [39], although the details depend on both eigenvalue ratios ρ and δ_A. The simplest case is again $\rho > 1$: in this case, a single-stable periodic orbit becomes heteroclinic as $\sigma \downarrow 0$. When $0 < \rho < 1$, an infinite cascade of gluing bifurcations accumulates at $\sigma = 0$ from $\sigma > 0$ and does so at a geometric rate: $\sigma_{n+1}/\sigma_n = \exp -\pi\lambda_B/\omega_B$. At these bifurcations, a pair of asymmetric orbits glues to form a symmetric orbit or a symmetric orbit splits into two asymmetric ones, depending on whether n is even or odd. These orbits become increasingly more complex as n increases since n counts the number of half twists about the line BA. When $\delta_A > 1$ the orbits that glue are stable, but they are unstable (and degenerate) when $0 < \delta_A < 1$. However, regardless of the value of δ_A, each gluing bifurcation is preceded by a cascade of period-doubling bifurcations and chaos of Shil'nikov type. It should be emphasized that while asymmetric orbits undergo period-doubling cascades, the symmetric orbits must first undergo a bifurcation to asymmetry. We surmise that for the parameter values for which the direct numerical simulations were carried out the ratio $\rho > 1$. In this case, the repeated transients remain quasiperiodic as $\epsilon \downarrow \epsilon^*$, as observed in Figs. 5 and 9. Note that the ratio ρ depends on ϵ primarily through the eigenvalues α_B and λ_B both of which are small and so vary with ϵ dramatically. Thus, it is primarily the properties of the state B that are responsible for the presence or absence of chaotic repeated transients, and we use this fact as a justification for ignoring the imaginary parts of the eigenvalues α_A and λ_B. These introduce complications akin to those studied in Ref. [40].

[1] P. Kolodner, C. M. Surko, and H. Williams, Physica D **37**, 319 (1989).
[2] V. Steinberg, J. Fineberg, E. Moses, and I. Rehberg, Physica D **37**, 359 (1989).
[3] A. E. Deane, E. Knobloch, and J. Toomre, Phys. Rev. A **37**, 1817 (1988).
[4] J. Fineberg, E. Moses, and V. Steinberg, Phys. Rev. Lett. **61**, 838 (1988).
[5] P. Kolodner and C. M. Surko, Phys. Rev. Lett. **61**, 842 (1988).
[6] G. Dangelmayr and E. Knobloch, in *The Physics of Structure Formation*, edited by W. Güttinger and G. Dangelmayr (Springer-Verlag, New York, 1987), pp. 387–393; Nonlinearity **4**, 399 (1991); G. Dangelmayr, E. Knobloch, and M. Wegelin, Europhys. Lett. **16**, 723 (1991).
[7] M. C. Cross, Phys. Rev. A **38**, 3593 (1988); Physica D **37**, 315 (1989). These papers assume small group velocity and weak dispersive effects; these assumptions have been relaxed in the work of C. Martel and J. M. Vega, Nonlinearity **9**, 1129 (1996); **11**, 105 (1998).
[8] P. Kolodner, Phys. Rev. E **47**, 1038 (1993).
[9] O. Batiste, M. Net, I. Mercader, and E. Knobloch, in *Advances in Turbulence VIII*, edited by C. Dopazo (CIMNE, Barcelona, 2000), pp. 913–916; Phys. Rev. Lett. **86**, 2309 (2001).
[10] T. Clune and E. Knobloch, Physica D **61**, 106 (1992).
[11] H. Yahata, Prog. Theor. Phys. **85**, 933 (1991); L. Ning, Y. Harada, and H. Yahata, *ibid.* **97**, 831 (1997); D. Jacqmin and D. Heminger (unpublished).
[12] W. Barten, M. Lücke, W. Hort, and M. Kamps, Phys. Rev. Lett. **63**, 376 (1989); W. Barten, M. Lücke, M. Kamps, and R. Schmitz, Phys. Rev. E **51**, 5636 (1995). For a recent summary of this work, see M. Lücke, W. Barten, P. Büchel, C. Fütterer, St. Hollinger, and Ch. Jung, in *Evolution of Spontaneous Structures in Dissipative Continuous Systems*, edited by F. H. Busse and S. C. Müller (Springer-Verlag, Berlin, 1998), pp. 127–196.
[13] W. Barten, M. Lücke, and M. Kamps, in *Nonlinear Evolution of Spatio-temporal Structures in Dissipative Continuous Systems*, Vol. 225 of *NATO Series Advanced Studies Institute, B: Physics*, edited by F. H. Busse and L. Kramer (Plenum Press, New York, 1990), pp. 131–148.
[14] S. Hugues and A. Randriamampianina, Int. J. Numer. Methods Fluids **28**, 501 (1998).
[15] S. Zhao and M. J. Yedlin, J. Comput. Phys. **113**, 215 (1994).
[16] O. Batiste, I. Mercader, M. Net, and E. Knobloch, Phys. Rev. E **59**, 6730 (1999).
[17] W. Schöpf and W. Zimmermann, Europhys. Lett. **8**, 41 (1989).
[18] Strictly speaking, this bifurcation is a Neimark-Sacker bifurcation. However, in the following we do not distinguish between Hopf bifurcations of equilibria and of periodic orbits, since resonance phenomena appear to play little role in the observed dynamics.
[19] P. C. Hirschberg and E. Knobloch, Physica D **90**, 56 (1996).
[20] E. Knobloch, in *Pattern Formation: Symmetry Methods and Applications*, edited by J. Chadam, M. Golubitsky, W. F. Langford and B. Wetton (Fields Institute, Toronto, 1996), Vol. 5, pp. 271–279.
[21] A. Arnéodo, P. Coullet, and C. Tresser, Phys. Lett. A **81**, 197 (1981).
[22] J. Guckenheimer, in *Dynamical Systems and Turbulence*, Vol. 898 of Springer Lecture Notes in Mathematics, edited by D. A. Rand and L. S. Young (Springer-Verlag, New York, 1981), pp. 99–142; SIAM (Soc. Ind. Appl. Math.) J. Math. Anal. **15**, 1 (1984).
[23] E. Knobloch and D. R. Moore, Phys. Rev. A **42**, 4693 (1990).
[24] V. Kirk, Phys. Lett. A **154**, 243 (1991); Physica D **66**, 267 (1993).
[25] E. Knobloch, D. R. Moore, J. Toomre, and N. O. Weiss, J. Fluid Mech. **166**, 409 (1986).
[26] C. Grebogi, E. Ott, and J. A. Yorke, Phys. Rev. Lett. **51**, 339 (1983).
[27] D. Ruelle and F. Takens, Commun. Math. Phys. **20**, 167 (1971); *ibid.* **23**, 343 (1971).
[28] M. Renardy, Fluid Dyn. Res. **24**, 189 (1999).
[29] E. Kaplan, E. Kuznetsov, and V. Steinberg, Phys. Rev. E **50**, 3712 (1994); Europhys. Lett. **28**, 237 (1994).
[30] J. J. Niemela, G. Ahlers, and D. S. Cannell, Phys. Rev. Lett. **64**, 1365 (1990).
[31] M. Bestehorn, R. Friedrich, and H. Haken, Z. Phys. B: Condens. Matter **77**, 151 (1989).
[32] A. S. Landsberg and E. Knobloch, Phys. Rev. E **53**, 3579 (1996).
[33] J. Moehlis and E. Knobloch, Phys. Rev. Lett. **80**, 5329 (1998).
[34] T. S. Sullivan and G. Ahlers, Phys. Rev. A **38**, 3143 (1988).
[35] J. Guckenheimer and P. Holmes, *Nonlinear Oscillations, Dynamical Systems and Bifurcations of Vector Fields* (Springer-Verlag, New York, 1984).
[36] V. Kirk (private communication).
[37] S. M. Tobias, N. O. Weiss, and V. Kirk, Mon. Not. R. Astron. Soc. **273**, 1150 (1995).
[38] A. M. Rucklidge and P. C. Matthews, Nonlinearity **9**, 311 (1996).
[39] P. Glendinning and C. Sparrow, J. Stat. Phys. **35**, 645 (1984).
[40] A. C. Fowler and C. T. Sparrow, Nonlinearity **4**, 1159 (1991).